VSEBINA – CONTENTS

THE INTERACTION OF SOFC ANODE MATERIALS WITH CARBON MONOXIDE

REAKCIJE MED ANODNIMI MATERIALI SOFC IN OGLJIKOVIM MONOKSIDOM

Barbara Novosel[1], Mihael Avsec[2], Jadran Maček[1]

[1]Faculty of Chemistry and Chemical Technology, University of Ljubljana, Aškerčeva 5, 1000 Ljubljana, Slovenia
[2]CHEMASS, Babičeva ul. 1, 1000 Ljubljana, Slovenia
barbara.novosel@fkkt.uni-lj.si

High-temperature solid-oxide fuel cells (SOFCs) are modern systems used for the transformation of chemical energy into electrical energy. The main problem in their development is related to the materials used for their construction, e.g., electrodes, electrolytes, interconnects, etc. The ageing of the electrocatalysts, the anode and the cathode, produces microstructural changes due to the high operating temperature, and in the case of the internal steam reforming of the fuel, due to the interaction of the anode material in contact with the gaseous phase. In the latter case, deactivation of the anode is caused by the deposition of carbon, which hinders the fuel transport on, and in, the porous anode. This carbon deposition is the consequence of the methane dehydrogenation reaction or Boudouard´s equilibrium reaction. The reaction of carbon monoxide with the anode material is the focus of the present study.
A composite anode material made of nickel and yttria-stabilized zirconia was exposed in a micro-reactor, at different temperatures, to a gas mixture of carbon monoxide (4 %) and argon (96 %). Depending on the cermet sample and the conditions in the micro-reactor, Boudouard's equilibrium was established, accompanied by the formation of carbon deposits. The amount of carbon deposited and its reactivity was determined later by a temperature-programmed oxidation in air. The interval of the oxidation temperature for carbon isothermally deposited at temperatures of 400 °C, 500 °C, 600 °C and 700 °C was found to lie in the temperature range from 476 °C to 610 °C. Less-reactive forms of carbon were obtained by depositing at higher temperatures. The changes in the composition of the gas phase in contact with the anode material were followed by on-line coupled mass spectrometry and gas chromatography.

Key words: carbon deposition, carbon monoxide, Boudouard's equilibrium, SOFC

Visokotemperaturne gorivne celice SOFC so sodobni sistemi za pretvorbo kemične v električno energijo. Glavni problem pri njihovem razvoju so konstrukcijski materiali, kot so elektrode, elektrolit, vmesnik idr. S staranjem elektrokatalizatorjev, anode in katode nastajajo mikrostrukturne spremembe zaradi visoke delovne temperature in interakcije anodnega materiala s plinsko fazo v primeru parnega reforminga goriva. Sčasoma se pojavi deaktivacija anode, zaradi nanosa ogljika, ki ovira transport goriva na in v pore anode. Nanesen ogljik je posledica reakcije dehidrogenacije metana ali reakcije Boudouardovega ravnotežja. Reakcija ogljikovega monoksida z anodnim materialom je predmet predloženega dela.
Kompozitni anodni material niklja in stabiliziranega itrijevega oksida je bil v mikroreaktorju izpostavljen plinski zmesi ogljikovega monoksida (4 %) in argona (96 %) pri različnih temperaturah. V odvisnosti od kermetnega materiala in razmer v mikroreaktorju se je vzpostavilo Boudouarjevo ravnotežje s sočasnim nanosom ogljika. Količina nanesenega ogljika in njegova reaktivnost je bila določena kasneje s temperaturno programirano oksidacijo v zraku. Temperaturni interval oksidacije ogljika, ki je bil nanesen v izotermnih razmerah pri 400 °C, 500 °C, 600 °C in 700 °C, je v temperaturnem območju med 476 °C in 610 °C. Manj reaktivne oblike ogljika so nastajale pri nanosu pri višji temperaturi. Spremembe sestave plinske faze pri kontaktu z anodnim materialom smo spremljali z masno spektrometrijo in plinsko kromatografijo.

Ključne besede: nanos ogljika, ogljikov monoksid, Boudouardovo ravnotežje, SOFC

1 INTRODUCTION

The main advantage of SOFCs with respect to other types of energy converters is the possibility of using methane and other hydrocarbons, even biogas derived from biomass gasification, as fuels [1]. This is enabled by conducting internal steam reforming and water gas shift reactions in the anode layer of the SOFC membranes:

$$CH_4 + H_2O \rightarrow CO + 3H_2 \qquad (1)$$

$$CO + H_2O \rightarrow CO_2 + H_2 \qquad (2)$$
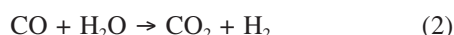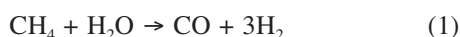
Some undesired side reactions can occur that lead to carbon deposition on, and in, the porous anode [2]:

$$CH_4 \rightarrow C + 2H_2 \qquad (3)$$

$$2CO \rightarrow C + CO_2 \qquad (4)$$

$$CO + 2H_2 \rightarrow C + CO_2 \qquad (5)$$

The material deposited according to reaction (3) is usually called coke, and that deposited by reaction (4), carbon [3]. In coke, besides carbon, also some heavier polymeric hydrocarbon chains are found [4]. The problems associated with carbon deposition were known from the beginning of the research on SOFCs, and even before that the petrochemical industry had similar problems with steam-reforming processes. In these processes methane (or a heavier hydrocarbon) is reacted with steam in a molar ratio of at least 2:1 (H_2O:CH_4). In the presence of a nickel catalyst at temperatures of 800 °C or above, a synthesis gas consisting of a mixture of hydrogen and carbon monoxide is produced. During the prolonged operation of the steam reformer, carbon deposits occur but in a petrochemical plant they are easily dealt with by flushing the catalyst with steam and

thus converting the deposits to carbon monoxide and hydrogen. In the case of fuel cells the anode material consists in most cases of a nickel cermet, the ceramic matrix being yttria-stabilized zirconia. Regeneration by steam flushing is not appropriate since it can lead to the reoxidation of the nickel to nickel oxide and an associated volume expansion of the nickel phase that can impair the anode layer. The greater sensitivity of the anode layer to the harmful effect of steam flushing results from dimensional and functional factors. The thickness of the anode layer ranges from several tens of micrometers to several hundred micrometers in the case of an anode-supported cell, as compared to catalyst particles for industrial steam reforming that are in the range of centimetres. Any volume expansion in the anode layer can lead to cracking and delamination from the electrolyte layer. Even minor changes in the micro-morphology of the anode can also lower its conductivity.

Carbon deposition problems for SOFCs running on hydrocarbons are usually dealt with by an appropriate steam-to-carbon ratio of more than 2 : 1. For the commercial use of SOFCs the expected lifetime of a cell is very important. Besides solving problems associated with the ageing and poisoning of the cell's electro-catalysts, the prevention of coking is of utmost importance and can markedly enhance the lifetime of the cell, which should be 40,000 h or more [5].

2 EXPERIMENTAL

The samples of anode material, i.e., a composite of nickel and yttria-stabilized zirconia (Ni/YSZ), were of commercial origin. The sample designated as FCM was a nickel oxide and yttria-stabilized zirconia powder (with mass fractions 66 % NiO and 34 % YSZ-8 (mole fraction 8 % Y_2O_3), with a surface area of 5.65 m²/g) from Fuel Cell Materials, OH, USA. Sample IAM was obtained from Inframat® Advanced Materials, USA, Nanox 28ZY8-1 (sample volume fractions of composition Ni/YSZ 50/50 %, surface area 66.87 m²/g). For baseline measurements Tosoh – Zirconia TZ-8Y yttria-stabilized zirconia powder, from the Tosoh Corporation, Japan was used.

The gases were simultaneously analysed by an Inficon Quadrex 200 mass spectrometer (input pressure 1 mbar, head pressure $3.3 \cdot 10^{-6}$ mbar, or $6.6 \cdot 10^{-6}$ mbar, gain $6 \cdot 10^{-11}$ A, scan time 2.703 s, scanning borders 0–50 amu) and Agilent Micro GC 3000A gas chromatograph (carrier gas argon 5.0, analytical columns: Plot U, Plot Q with timed controlled injector and molecular sieve with backflush input, detector type: TCD, inlet temperature 140 °C, injector temperature 100 °C, column temperature 100 °C for Plot U, 70 °C for Plot Q and 80 °C for molecular sieve, column pressure 2.068 bar for Plot U and Plot Q, 2.206 bar for molecular sieve, analysis run

time 180 s). The testing system set-up has been described elsewhere [6].

The amount of deposited carbon was determined by temperature-programmed oxidation of a known amount (1.5 mg) of carbon (soot Printex) in the testing system. By determining the area under the carbon dioxide curve obtained by integration, the correlation factor was obtained and used for quantification of the MS and GC results.

3 RESULTS AND DISCUSSION

The deposition of carbon on the SOFC anode can be attributed to three main reactions (3-5) and depends on the conditions in the cell, e.g., the steam-to-fuel ratio, the temperature, the flow rate etc., as well as on the anode material and its characteristics (composition and micro-morphology). More research has been done on coke deposition from hydrocarbon fuels (3) and less on carbon deposition from the carbon monoxide disproportionation reaction (4). The well-known Boudouard's equilibrium implies that at higher temperatures carbon monoxide will be stable and that at lower temperatures the deposition of carbon can be expected. A general trend in SOFC development is lowering of the operating temperature of the cell, which ten years ago was approximately 1000 °C. Nowadays the operating temperatures have dropped to 750 °C and even lower values have been mentioned in the literature [7,8]. This is within the temperature region where carbon deposition is expected and this research work was directed towards studying this phenomenon.

The carbon deposition was tested with contacting samples of anode material in powdered form with a mixture of the volume fraction of carbon monoxide (4 %) and argon (96 %) under temperature-programmed and isothermal conditions. The anode materials were characterized with electron microscopy and specific-surface-area measurements. The FCM material is a fine powder with an average particle size below one micrometer. The IAM material differs appreciably in particle size, which is several ten micrometers of the agglomerates of smaller particles. The specific-surface-area measurements show a roughly tenfold difference between the two samples. Although it could be expected that the finer material would have a larger specific area, this was not the case, the FCM sample had 5.65 m²/g and the IAM sample, 66.87 m²/g, which can be attributed to the porosity of the agglomerated particles in this sample.

The carbon deposition was followed by a system for determining the interaction of solid materials with the gaseous phase [6]. The system consisted of a gas-supply system, a furnace with a quartz micro-reactor and a temperature controller, a quadrupole mass spectrometer, gas chromatograph and PC where all the data are collected and stored. In the case of studies of the dehydrogenation of methane, the evolution of hydrogen was monitored as a measure of carbon deposition, while

for the carbon monoxide disproportionation reaction carbon dioxide was determined. Gas-analysis methods were chosen because of their sensitivity compared to thermogravimetry and other analytical techniques.

The testing protocol began with the temperature-programmed reduction (TPR) of the sample in an argon/hydrogen mixture for converting nickel oxide to metallic nickel, followed by cooling of the furnace to room temperature in the same atmosphere. The second phase was either the temperature programmed (TPD) or the isothermal deposition (ITD) of carbon from the argon/carbon monoxide mixture. The third step, after cooling the sample to room temperature, was the temperature-programmed oxidation (TPO). This set of experiments was carried out on the anode materials to find which one was less susceptible to carbon deposition. Therefore, the conditions for higher rates of carbon deposition, achieved by omitting the addition of steam into the gas stream, were created intentionally.

The carbon deposition on a fuel cell occurs mainly due to reactions (3) and (4). For comparison TPD was also carried out from a mixture of methane with argon, leading to coking of the electrocatalyst [9]. In this case carbon deposition follows the reaction path (3) and the hydrogen concentration in the carrier gas is a measure of the carbon deposited (**Figure 1**).

This figure shows that on the FCM sample no carbon was deposited until a temperature of 439 °C was reached, when the heterogeneous thermal dissociation of methane according to reaction (3) started. At 527 °C the maximum concentration of hydrogen was observed. With a further increase in the temperature, the hydrogen
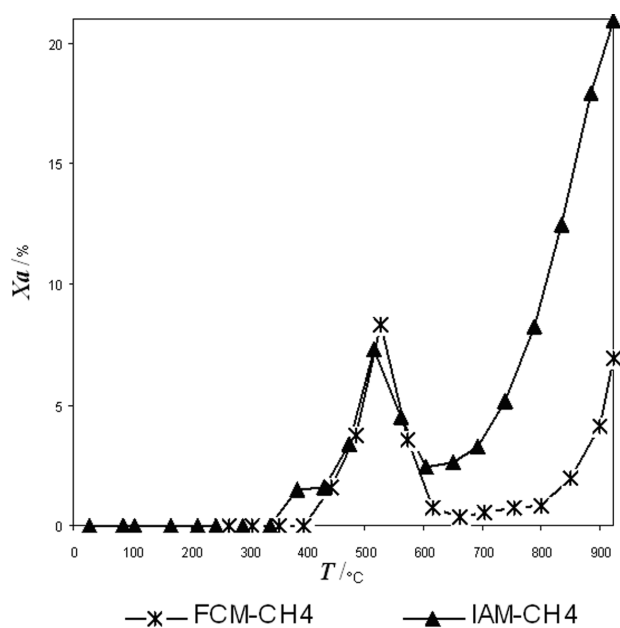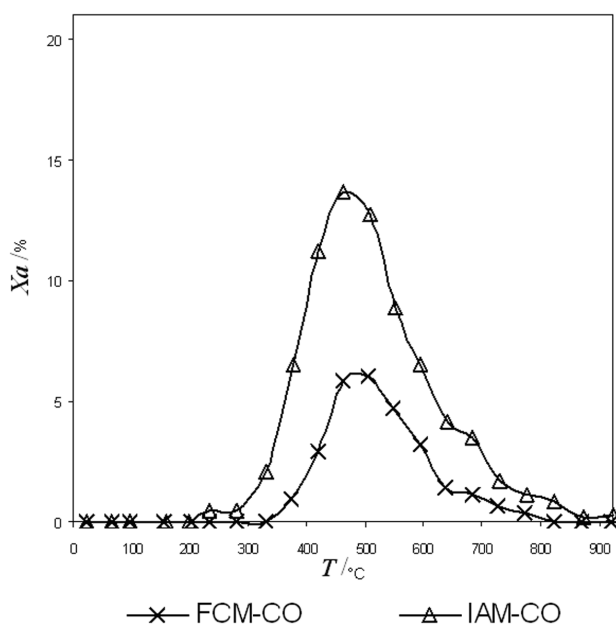

Figure 2: Deposition from carbon monoxide, degree of conversion of CO vs. Temperature
Slika 2: Nanos iz ogljikovega monoksida; stopnja konverzije CO v odvisnosti od temperature

concentration decreased and reached a minimum at 661 °C. Up to 800 °C the hydrogen concentration stayed almost at the same low level and above this temperature it rose more steeply again. The IAM sample behaved similarly but with a small preceding peak before the larger one at 337 °C. In this case also the hydrogen concentration above this temperature decreased again, but it never reached such low values as in the case of FCM and it started to rise much more steeply after 694 °C. We assume that for the first peak coverage of the active sites on the nickel particles occurred. With increasing temperature the carbon starts to deposit over the whole material and onto already deposited carbon, accompanied by an intensive evolution of hydrogen.

The deposition of carbon from the disproportionation reaction of carbon monoxide (4) was carried out initially with the aim to obtain an overview of the system using a dynamic test with temperature-programmed heating of both samples up to 930 °C in an argon/carbon monoxide mixture. The deposition of carbon was followed by measuring the concentration of carbon dioxide in the carrier gas according to reaction (4). For sample FCM the evolution of carbon dioxide started at 374 °C and reached a maximum concentration at 505 °C (**Figure 2**). The rate of CO_2 evolution changed again at 637 °C and decreased practically to zero at 822 °C. In the case of the IAM sample the first evolution of carbon dioxide occurred at 232 °C. A small peak preceded a much larger one. The highest carbon dioxide concentration was obtained at 464 °C. With increasing temperature the carbon dioxide concentration diminished with two distinctive shoulders at 639 °C and 730 °C. The

Figure 1: Deposition from methane, degree of conversion of CH_4 vs. temperature
Slika 1: Nanos iz metana; stopnja konverzije CH_4 v odvisnosti od temperature

maximum conversion of carbon monoxide into dioxide was twice that of the IAM sample.

Isothermal deposition tests (ITD) were made at temperatures of 400 °C, 500 °C, 600 °C and 700 °C. The samples were first heated in an argon atmosphere. After the pre-selected temperature was reached, the furnace was set to the isothermal mode and the atmosphere was exchanged for a mixture of carbon monoxide and argon. After 80 minutes of deposition the atmosphere was again changed to argon and the furnace cooled down to room temperature. The result the ITD sample gave was the curves for carbon dioxide concentration in the carrier gas vs. time. The general shapes of the curves for both samples are similar, with significant differences in the peak concentration and the decay line. The carbon dioxide concentration first steeply increased and in approximately 5 min reached its maximum. The peak height for the FCM sample was the highest for carbon deposited at 500 °C followed by 400 °C, 700 °C and 600 °C (**Figure 3**). With increasing temperature the concentration falls off, but at different rates. For all the samples the curves almost level off after 80 min. Although the concentration of carbon dioxide levels off it does not return to zero even after 80 min. The concentration of carbon dioxide remaining in the carrier gas is very similar for three temperatures but more than twice as high for the sample prepared at 600 °C. The IAM anode material shows a similar behaviour (**Figure 4**). The peak carbon dioxide concentrations follow the same order as for the FCM sample, but appreciably different decay curves were observed. The sample obtained at 600 °C levels off first, followed by the one prepared at 700 °C. The residual concentration of carbon dioxide is more than three times as high for the sample prepared at 600

°C than for the one prepared at 100 °C higher. The samples prepared at 500 °C and 400 °C do not reach the level of constant CO_2 concentration. In all four cases the deposition proceeds even after 80 min.

The ITD follows the expected pathway. When carbon monoxide comes into contact with fresh anode material, the deposition abruptly starts to produce a very sharp peak.

Samples with deposited carbon prepared during the isothermal deposition tests were left in quartz micro-reactors to cool down. After the atmosphere was changed to dry air, they were reheated in the temperature-programmed mode to 800 °C.

The TPO of the samples provides us with several data, e.g., the initial temperature of the carbon oxidation, the temperature interval in which it is oxidized and the amount of carbon deposited. During TPO carbon is oxidized to dioxide and transferred by the carrier gas to GC and MS. The results of the temperature-programmed oxidation for both samples are presented in **Figures 5 and 6**. Carbon was deposited from 400 °C to 700 °C in 100 °C increments. The TPOs of the FCM reveal three different curves for the deposited carbon. That obtained at 400 °C oxidizes at 517 °C producing a small peak (compared to the others). Carbon deposited at 500 °C and 600 °C oxidizes at 520 °C and 555 °C, respectively, producing sharp and narrow peaks. Carbon deposited at 700 °C produces a very broad peak extending over a wide temperature interval. The amount of carbon dioxide released was appreciably lower than in the other cases, so the results for this curve were obtained by GC instead of by MS which was used in the other three instances.

A comparison was made of the FCM results and those obtained for the second material. The IAM shows a
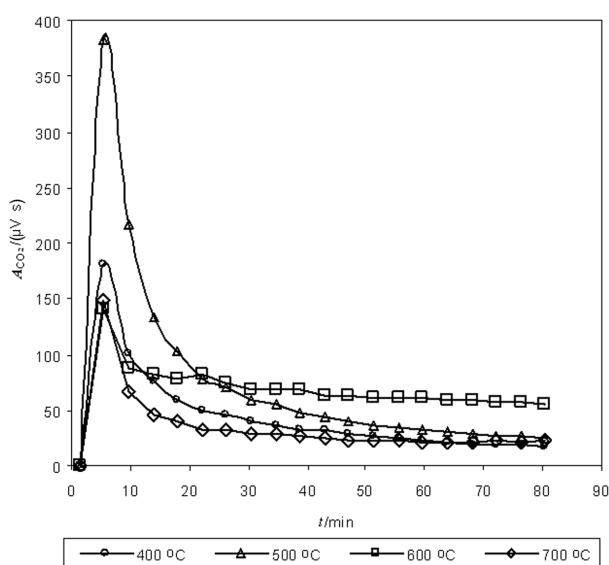

Figure 3: TPD of FCM sample at different temperatures, $A_{CO2}/(\mu V\ s)$ GC signal
Slika 3: TPD vzorca FCM pri različnih temperaturah, $A_{CO2}/(\mu V\ s)$ za GC signal
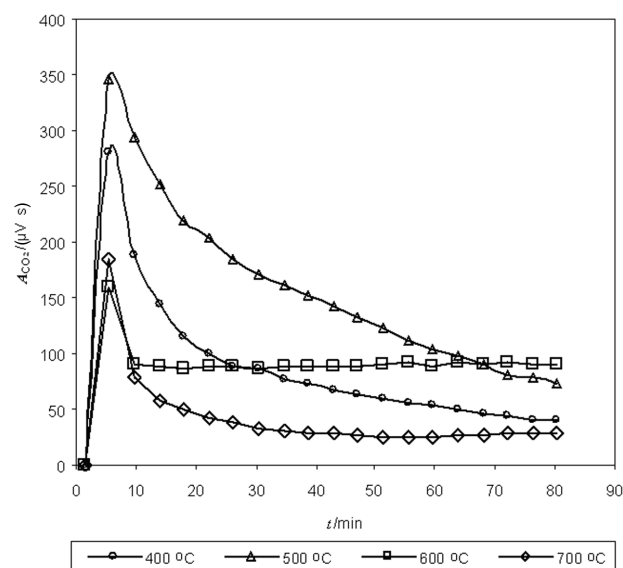
Figure 4: TPD of IAM sample at different temperatures, $A_{CO2}/(\mu V\ s)$ GC signal
Slika 4: TPD vzorca IAM pri različnih temperaturah, $A_{CO2}/(\mu V\ s)$ za GC signal
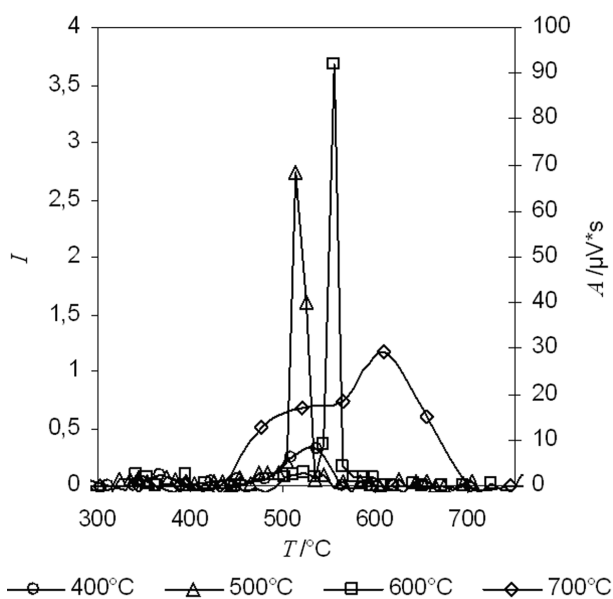
Figure 5: CO_2 evolution during TPO of carbon previously deposited at 700 °C on FCM sample/I – intensity of MS signal, A/(μV s) GC signal

Figure 5: Sproščanje CO_2 med TPO ogljika predhodno deponiranega pri 700 °C na vzorcu FCM/I – intenziteta za MS signal, A/(μV s) za GC signal
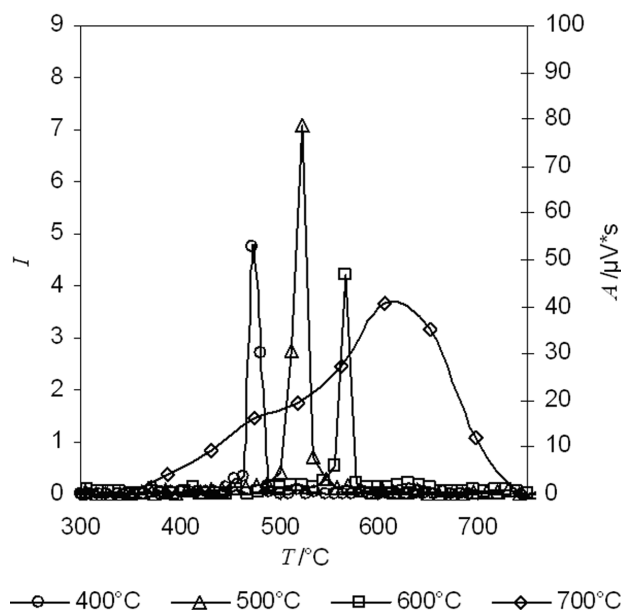

Figure 6: CO_2 evolution during of carbon previously deposited at 700 °C on IAM sample/I – intensity of MS signal, A/(μV s) GC signal

Figure 6: Sproščanje CO_2 med TPO ogljika predhodno deponiranega pri 700 °C na vzorcu IAM/I – intenziteta za MS signal, A/(μV s) za GC signal

similar outcome (**Figure 6**). The greatest difference between the two sets of data is in the initial temperature and the height of the peak for deposition at 400 °C. For the IAM sample this peak is large and sharp with a peak temperature of 476 °C. The positions of the peaks for the samples obtained at 500 °C and 600 °C do not change significantly on the temperature scale. The peak for the IAM sample deposited at 700 °C again differs appreciably from the other three, although the shape is similar to the one obtained at the same temperature for the FCM sample. It also shows a bimodal shape but extends across

an even wider temperature interval, from 342 °C to 742 °C.

A comparison of the masses of carbon deposited per mg of sample shows that at all four temperatures the amount of deposited carbon is from 1.7 to 3.5 times higher in the case of the IAM sample (**Table 1**). The greatest discrepancy is at the lowest temperature of deposition. This is in accordance with the specific-surface-area measurements, where the IAM sample has around a tenfold larger specific area than the FCM sample.

Table 1: Amount of deposited carbon
Tabela 1: Količina nanesenega ogljika

	FCM sample			IAM sample			IAM:FCM
$T_{deposition}$	$m_{Ni\text{-}YSZ}$	m_C	$m_C/m_{Ni\text{-}YSZ}$	$m_{Ni\text{-}YSZ}$	m_C	$m_C/m_{Ni\text{-}YSZ}$	$m_{C\text{-}IAM}/m_{C\text{-}FCM}$
(°C)	(mg)	(mg)	(10^{-3})	(mg)	(mg)	(10^{-3})	(10^{-2})
400	41.82	0.228	5.4	43.28	0.832	19.2	3.5
500	41.93	0.619	14.8	42.18	1.818	43.1	2.9
600	43.19	0.576	13.3	42.40	0.938	22.1	1.6
700	41.70	0.098	2.3	42.24	0.173	4.1	1.8

Table 2: Temperature of oxidation of carbon deposits
Tabela 2: Temperatura oksidacije nanesenega ogljika

	FCM sample				IAM sample			
$T_{deposition}$	$T_{initial}$	T_{peak}	T_{end}	$T_{end}-T_{initial}$	$T_{initial}$	T_{peak}	T_{end}	$T_{end}-T_{initial}$
(°C)	(°C)	(°C)	(°C)	(°C)	(°C)	(°C)	(°C)	(°C)
400	475	517	567	92	436	476	493	57
500	445	520	550	105	465	520	587	122
600	491	555	606	115	479	569	650	171
700	432	609	700	268	342	652	742	320

The TPO results show more than just the amount of deposited carbon, and from these data, and especially its oxidation temperature, conclusions about the reactivity of the deposit may be drawn (**Table 2**). With other parameters being the same or at least similar, the oxidation temperature of the carbon deposited on the sample mainly depends on the allotropic form of the carbon, the particle size, the shape and the porosity. Graphite is less reactive towards oxidation than soot [6]. A higher reactivity of carbon is advantageous since it increases the possibility that it will react with water vapour.

It is known that carbon species deposited at lower temperatures exhibit a higher reactivity than those deposited at higher temperatures [10]. From our data it can be concluded that at 700 °C the mechanism and the product of this deposition reaction are significantly different from those obtained at 600 °C. For the FCM sample 6.1 times less carbon is deposited at 700 °C than at the previous temperature of 600 °C, and for the IAM sample the value is 5.4 times less. The very broad peak of the bimodal shape could also indicate that several carbon species with different reactivities are deposited.

The above-mentioned trend for lowering the operating temperatures of SOFCs will simplify the choice of materials for them and reduce some constructional problems, but it may also enhance the carbon deposition rate and the associated problems. The carbon deposition from carbon monoxide disproportionation may occur not only during the operation but also during the startup and shutdown of the cells when the system passes through temperature regions where carbon deposition is favoured.

The catalytic effect of the anode material on the fuel has already been studied, but in SOFCs running on the internal reforming mode it is also important to know its effect on the Boudouard equilibrium reaction. By determining the reactivity of carbon from different sources, i.e., reactions, it is possible to predict which form has the most detrimental effect on the operation of the cell. Even if the contribution to the deposition of carbon from Boudouard's reaction is not dominant in terms of mass, the early formation of stable nuclei can speed up the deposition by hydrocarbon dehydrogenation.

Complex equilibria are established between the gases in the porous anode material, with some of the reactions leading to carbon deposition. In spite of the strong interrelationship between the reactions occurring in the anode, they can nevertheless be studied individually and the contribution of each to the whole system determined. It is important to know which reaction contributes most to the formation of deposits, what is the nature of the deposit and if a suitable change in the composition and the micro-morphology can diminish it.

The conditions used for the tests presented in this study are not the same as those in the anode during its operation. It is desirable that all nickel particles are connected with adjacent nickel particles and similarly also all YSZ particles are part of an interconnected 3D network, which enables the transfer of oxygen ions in the depth of the anode. The main difference between our conditions and those in the fuel cell is the absence of a flow of oxygen ions into the anode and the electron transfer out of it. The conditions at a particular micro-location can, however, be similar to ours because all of the particles of both phases are not a part of such a continuum. The presence of water vapour was intentionally omitted to speed up the deposition rate and shorten the duration of the experiments. In order to carry out the tests under more realistic conditions, it should be introduced into the system and thus the results under dry conditions verified.

4 CONCLUSION

Studies of carbon deposition on the anodes of high-temperature fuel cells using internal fuel reforming usually deal with the overall deposition from two main contributions, i.e., the carbon from hydrocarbon dehydrogenation and the carbon monoxide from disproportionation reactions. The system carbon-monoxide-Ni/YSZ anode material was studied with the aim of learning more about its contribution to the overall carbon deposition process and the influence of the anode material on Boudouard's equilibrium.

There are substantial differences in the carbon deposition on the FCM and IAM samples. In dynamic carbon-deposition tests the IAM starts to catalyze the disproportionation of carbon monoxide at lower temperatures and gives a twofold amplitude for this conversion compared to FCM. The IAM sample has a 10 times larger specific surface area than the FCM, and that is probably the reason for its greater activity.

A comparison of the mass of carbon deposited per mg of sample shows that at all four temperatures the amount of carbon deposited is from 1.6 to 3.5 times higher in the case of the IAM sample, with the largest difference between the two samples at the lowest temperature of 400 °C.

The amount of carbon deposited, however, does not represent the only measure of the suitability of materials and conditions that prevail in the anode. The deposition at 700 °C showed that very little carbon was formed and that it, or at least part of it, is reactive enough for the oxidation reaction, while the other part is very stable and does not oxidize up to very high temperatures.

Studies of the carbon deposition on powdered samples of anode materials and their results must be carefully used for the correlation or interpretation of the processes that occur in the anode of a working SOFC. In this study there is no flow of oxygen ions through the electrolyte into the anode and therefore also no electrochemical reactions. Nevertheless, a selective study of

partial reactions and their contribution to the overall deposition can supply valuable data that can be used for designing materials for better and more coke/carbon-resistant anodes.

Acknowledgement

5 REFERENCES

[1] Eguchi, K., Kojo, H., Takeguchi, T., Kikuchi, R., Sasaki, K.: Fuel flexibility in power generation by solid oxide fuel cells, Solid State Ionics 152–153 (**2002**), 411–416

[2] Huang, T.-J., Wang, C.-H.: Factors in forming CO and CO_2 over a cermet of Ni-gadolinia-doped ceria with relation to direct methane SOFCs, Journal of Power Sources 163 (**2006**), 309–315

[3] Bartholomew C. H.: Mechanisms of catalyst deactivation, Applied Catalysis A: General, 212 (**2001**), 17–60

[4] Triantafyllopoulos, N. C., Neophytides, S. G.: The nature and binding strength of carbon adspecies formed during the equilibrium dissociative adsorption of CH_4 on Ni–YSZ cermet catalysts, Journal of Catalysis, 217 (**2003**) 324–333

[5] Tu, H., Stimming, U.: Advances, aging mechanisms and lifetime in solid-oxide fuel cells, Journal of Power Sources, 127, (**2004**) 1–2, 284–293

[6] Maček, J., Novosel, B., Marinšek, M. Ni-YSZ SOFC anodes: minimization of carbon deposition. J. Eur. Ceram. Soc. [Print ed.], 27 (**2007**), 487–491

[7] Chen, F., Zha, S., Dong, J., Liu, M.: Pre-reforming of propane for low-temperature SOFCs, Solid State Ionics 166 (**2004**), 269–273

[8] Leng, Y. J., Chan, S. H., Jiang, S. P., Khor, K. A.: Low-temperature SOFC with thin film GDC electrolyte prepared in situ by solid-state reaction, Solid State Ionics 170 (**2004**), 9–15

[9] Takeguchi, T., Kani, Y., Yano, T., Kikuchi, R., Eguchi, K., Tsujimoto, K., Uchida, Y., Ueno, A., Omoshiki, K., Aizawa, M.: Study on steam reforming of CH_4 and C_2 hydrocarbons and carbon deposition on Ni-YSZ cermets, Journal of Power Sources, 112 (**2002**), 588–595

[10] Finnerty, C. M., Coe, N. J., Cunningham, R. H., Ormerod, R. M.: Carbon formation on and deactivation of nickel-based/zirconia anodes in solid oxide fuel cells running on methane, Catalysis Today, 46 (**1998**), 137–145

LUBRICATION FLOW DURING THE ROLLING OF SEAMLESS TUBES

TOK MAZIVA PRI VALJANJU BREZŠIVNIH CEVI

Dušan Ćurčija[1], Ilija Mamuzić[2]

[1]Kneza Branimira 7, 44103 Sisak, Croatia
[2]Metallurgical faculty, University of Zagreb, Aleja narodnih heroja 3, 44103 Sisak, Croatia

An approximate analytical solution for calculating the lubricant-layer thickness for the continuous rolling of seamless tubes on a long, floating mandrel was derived. In the area of nano-behavior, the geometry of the process prevails over the rheological and kinematic characteristics. The solutions were derived for tools and tubes with smooth surfaces and offer the possibility of optimizing the quality of the lubricant. In calculations of the nano-lubricant layer, the thickness is assumed to be an artificial irrational value for maintaining the continuity of the mathematical analysis. This analysis justifies the use of new geometrical characteristics for the mandrel.

Key words: seamless tubes, rolling, lubrication

Razvita je bila približna analitska rešitev za izračun debeline maziva pri neprekinjenm valjanju brezšivnih cevi na plavajočem trnu. V območju nano obnašanja geometrija procesa prevlada nad reološkimi in kinematičnimi karakteristikami. Rešitev je razvite za orodja in cevi z gladko površinoin daje možnost za optimizacijo kakovosti maziva. Pri izračunu z nano debelino maziva, je debelina upoštevana kot umetna in irracionalna količina zaradi vzdrževanja kontinuitete matematične analize. Ta analiza opravičuje uporabo plavajočega trna z novo geometrijo.

Ključne besede: brezšivne cevi, valjanje, mazanje

1 INTRODUCTION

The rolling of tubes[1] in round passes is a variant of longitudinal rolling where, as a rule, and according to **Figure 1**, the two rolls and the mandrel form the zone of deformation[2]. The rolling with a long, floating mandrel occurs on a continuous rolling mill with seven to nine cages. Before the tube blank enters the rolling gap, a long, cylindrical mandrel is put into it, and then the mandrel moves in concordance with the rolled tube remaining in the zone of deformation. The mandrel's motion is slower than that of the tube front, but it is greater than the rate of the tube blank entering the gap between the rolls. The rolling speed is adjusted to obtain an equal speed of the tube and the rolls for every pass for a determined point of the cross-section of the deformation zone. In this way the curve of equal speeds of the tube and the rolls defines the range of relative sliding of metal, i.e., the zone of overtaking and the zone in arrears. It was proved experimentally[1] that during the rolling of the tube in several passes the overtaking takes place at the entrance of the tube in the gap between the rolls and the arrears at the exit of the gap between the rolls.

In recent years continuous rolling processes using long, fixed, cylindrical, conic or staged mandrels were developed. The rolling consists of two deformation zones: a zone for reduction of the tube's diameter, and a zone for the reduction of the tube's wall, as shown in **Figure 2**. No lubricant is added to the outside surface of the tube in contact with the rolls, and the friction[3] follows the Kulon-Amonton[4] law, while between the mandrel and the inside surface of the tube the friction occurs according to Newton's law. The tangential stress τ_x in the lubricant layer on the surface of the mandrel is described[5] by the differential equation:

$$\tau_x = \mu \cdot (v_C - v_T) \frac{1}{\varepsilon(x)} - \frac{1}{2} \varepsilon(x) \cdot \frac{\partial p}{\partial x} \qquad (1)$$

where μ is he dynamic viscosity of the lubricant, v_C and v_T are the speeds of the tube and the mandrel, $\varepsilon(x)$ is the
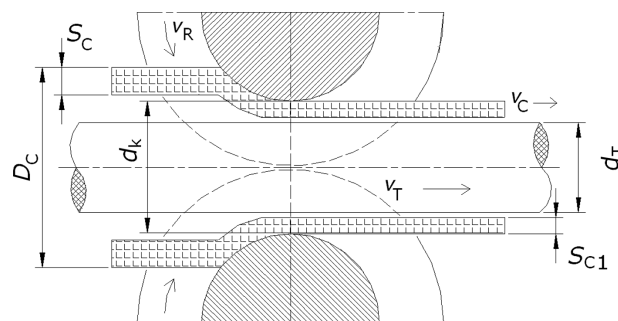
Figure 1: Scheme of rolling for seamless tubes on a long, floating mandrel: v_R – rolls peripheral velocity, v_T – mandrel motion velocity, v_C – tube motion velocity: S_C and S_{CI} – tube wall thickness before and after deformation, D_C; d_K, d_T, entrance and exit diameter of the tube and the diameter of mandrel

Slika 1: Shema valjanja brezšivnih cevi na dolgem plavajočem trnu: v_R – obodna hitrost valjev, v_T – hitrost premika trna, v_G – hitrost premika cevi, S_C in S_{C1} – vhodni in izhodni premer cevi in premer trna, D_C; d_K, d_T, vhodni in izhodni premer cevi in premer trna
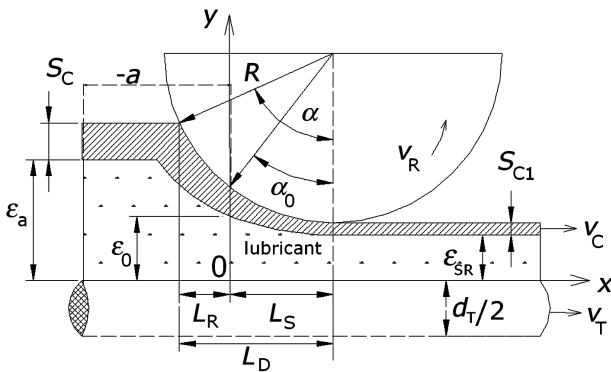
Figure 2: Two deformation sub zones in pass cross-section: L_R and L_S – zones of diameter and of wall reduction, ε_{SR} – average lubricant height on the mandrel in the last cage, α – engagement for tube blank pass angle, α_0 – angle of engagement deformation of the tube wall

Slika 2: Dve deformacijski podzoni na preseku prehoda: L_R in L_S – zoni redukcije premera in debeline stene, ε_{SR} – povprečna debelina maziva na trnu v zadnjem ogrodju, α – kot oprijema valjev na valjanec, α_0 – kot oprijema za deformacijo stene cevi

functional bond of the lubricant layer in Descartes coordinates, and $\partial p / \partial x$ is the partial gradient of the pressure in the lubricant layer along the x axis.

According[6] to **Figure 2**, for the lubricant consumption in the final cage of a continuous rolling mill, it is assumed that[7]:

$$\lim_{\varepsilon_a \to \varepsilon_0} (\alpha \to \alpha_0) \qquad (2)$$

where ε_o is the lubricant-layer thickness at the entrance cross-section of the wall reduction for the angle α_o, and ε_a is the lubricant-layer thickness on the floating mandrel in the zone of reduction of the wall of the tube.

2 MATHEMATICAL DESCRIPTION OF THE LUBRICATION

According to **Figure 2** the process of lubrication of the mandrel and of the inside surface of the tube is described by the following Osborn-Reynolds differential equation[8].

$$\frac{dp}{dx} = \frac{6\mu(\nu_C + \nu_T)}{\varepsilon^2(x)} - \frac{12\mu Q}{\varepsilon^3(x)} \qquad (3)$$

The specific consumption of lubricant per mandrel perimeter length is:

$$Q(x) = \int_0^{\varepsilon(x)} u\,dy = -\frac{1}{12\mu}\frac{dp}{dx}\varepsilon^3(x) + \left(\frac{(\nu_C + \nu_T)}{2}\right)\varepsilon(x) \quad (4)$$

where u is the average speed of the lubrication motion, and dp/dx is the change of pressure in the lubricant layer alongside the x axis.

The following relation determines the thickness of the lubricant layer:

$$\varepsilon(x) = \varepsilon_0 + R_0 \left[\cos\alpha_0 - \sqrt{1 - \left(\sin\alpha_0 - \frac{x}{R_0}\right)^2} \right] \qquad (5)$$

where $R_0 = R + S_{C1}$, R is the radius of the pass, and S_{C1} is the thickness of the tube wall in the last cage. The length of the lubricant wedge is calculated from:

$$a = R_0 \left[\sqrt{1 - \left(\cos\alpha_0 - \frac{\varepsilon_a}{R_0} + \frac{\varepsilon_0}{R_0}\right)^2} - \sin\alpha_0 \right] \qquad (6)$$

For the dressing processes the expression (5) can be developed to a power series:

$$\varepsilon(x) = \varepsilon_0 - \alpha_0 x + \frac{x^2}{2R_0} - \frac{\alpha_0 x^3}{2R_0^2} + \frac{x^4}{8R_0^3} \qquad (7)$$

In this paper the shape of the lubricant layer on the mandrel in the area of (–a; 0) will be treated analytically. It is of interest for practical applications, for deducing the optimal lubricant layer thickness and for savings of high-quality lubricant.

3 CALCULATION AND DISCUSSION

By inserting the tube blank into a round pass gap the engagement occurs in the gap outlet, and after that the whole pass is gradually filled. The deformation process and, first, the shape of the section of the tube is changed from round to oval. During the following pass, the oval blank is turned by 90° and the longer axis of the rolled tube section is engaged in the rolling gap. The rolling is then continued in this sequence to the final pass. In the first cages of the continuous rolling mill the lubrication is in surplus in front of the inlet cross-section of the zone of deformation, while in the last cage the lubrication is insufficient in front of the inlet cross-section of the zone of deformation, and the lubricant layer is worn off. The lubricant behavior is explained from considering the **Figures 3 and 4**.

For the conditions of von Mizes plasticity:

$$k = \sigma_T / \sqrt{3} \qquad (8)$$

where σ_T is the metal's deformation resistance and k is the constant of plasticity. The calculation will be developed on the basis of the pressure in the lubricant layer p_0 and the gripping angle of α.
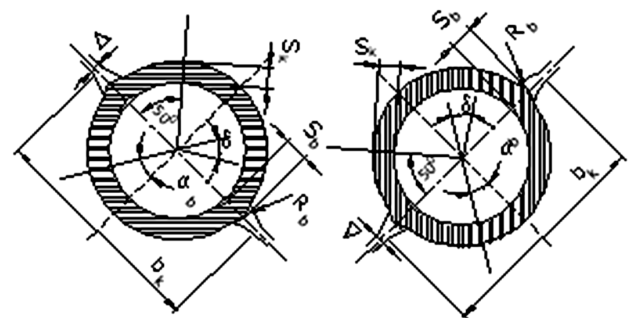
Slika 3: Okrogel prehod z zaokroženimi izhodi obrnjenimi za 90° v prvih dveh ogrodjih kontinuirne valjarne

Figure 3: Round pass with rounded outlets turned by 90° in the first two cages of the continuous rolling mill
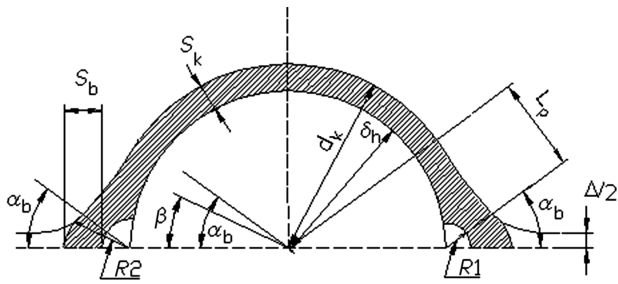
Figure 4: Detail of the round pass on the ninth cage of the continuous rolling mill $R1 \rightarrow R2 \rightarrow 0$. The wearing out of the lubricant is the most efficient at this rolling point.

Slika 4: Detail prehoda v devetem ogrodju kontinuirne valjarne $R1 \rightarrow R2 \rightarrow 0$. V tej točki valjanja je največja obraba maziva.

In **Table 1** the standard properties[9] of industrial lubricants according to the Russian standard C-24 (and data used for the following calculation) are given.

Table 1: The rheological, kinematic and geometric properties of lubricants[4,5]

Tabela 1: Reološke, kinematične in geometrične karakteristike maziv[4,5]

Parameter	Value	Unit
γ, pieso coefficient of viscosity	2.18E-7	Pa^{-1}
p_0, rolls pressure	20E6	Pa
v_C, motion speed of tube blank	8.5	m/s
v_T, mandrel speed	7.5	m/s
R, roll radius	0.197	m
S_{C1}	0.003	m
μ_0, dynamic viscosity of lubricant	0.024	Pa 8
α_0, engagement gripping angle	0–0.02	rad
ε_a, height of lubricant on the mandrel	0.001–0.0000001	m
A, technological parameter	1.965512E6	m^{-1}
$A = (1 - \exp(-\gamma \cdot p_0)/6\mu_0\gamma(v_C+v_T))$		
Smooth surfaces are assumed for the tube blanks and the mandrel $R_0 = R + S_{C1}$.		

The Barus dependence of lubricant viscosity on pressure is used, assuming a smooth surface for the mandrel and the tube:

$$\mu = \mu_0 \exp (\gamma \cdot p_0) \qquad (9)$$

The results of the calculation of lubricant-layer thickness ε_0 at the gripping point in dependence of the gripping angle α_0 for the last cage of the continuous mill for $\varepsilon_a > \varepsilon_0$ is shown in **Figure 5**. By increasing the dynamic viscosity of the lubricant, ε_0 is also increased. The change of thickness ε_0 for the final cages of the continuous rolling line is linear.

The dependence of ε_a on ε_0^1 for the wearing out of the lubricant in the last cage of the continuous rolling mill stand is given in **Figure 6**. Series 1 presents the case when $\varepsilon_a >> \varepsilon_0$, and Series 3 and 5 for the cases when ε_a is in the micro- and nano-ranges, respectively. With the
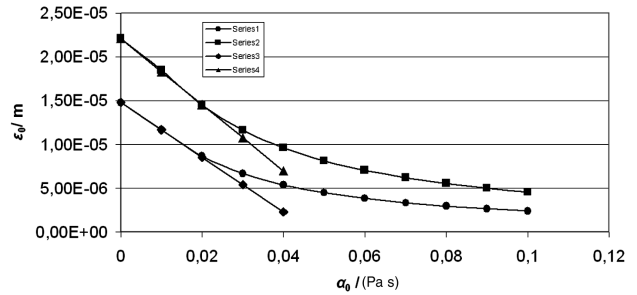

Figure 5: Influence of lubricant dynamical viscosity and the angle of engagement on the lubricant-layer thickness on the inlet cross-section of the wall-reduction zone

Series 1 – $\mu_0 = 0.024$ Pa s; Series 2 – $\mu_0 = 0.048$ Pa s; Series 3 and 4 – linearity through points $(0;\varepsilon_0^1)$ and $(\alpha_0^*; \varepsilon_0^*)$

Slika 5: Vpliv dinamične viskoznosti maziva in kota oprijema na debelino maziva na vhodnem preseku redukcije debeline stene cevi

Serija 1 – $\mu_0 = 0.024$ Pa s; Serija 2 – $\mu_0 = 0.048$ Pa s; Serije 3 in 4 – linearnost skozi točki $(0;\varepsilon_0^1)$ in $(\alpha_0^*; \varepsilon_0^*)$

entry in the nano-range, for example, for an extremely high intensity of lubrication wearing out, ε_0^1 practically does not undergo any changes when the dynamic viscosity of the lubricant increases. Then, the average thickness of the lubricant film ε_0 can determined if the final thickness of ε_0^1 is known.

In **Figure 7** the effect of $\Delta\varepsilon_0$ in the function $\varepsilon_a^{\wedge}(1/3)$ is shown. The C belongs to Series 2, and its maximum is less well expressed. In the graphical representation, four zones are distinguished:

• the φ-zone of the first operative cages of the continuous stand, characterized by $\varepsilon_a >> \varepsilon_0$;
• the Ω-zone of the *mili* area of the lubricant layer ε_a, characteristic for the right-hand side of the continuous stand with relation to the point M;
• the ϕ-zone of the center of the continuous stand in the environment, and after the point M when for the lubricant layer the thickness is on the boundary of hydrodynamic lubrication;
• the Σ-nano-zone characterized by intensive wearing of the lubricant on the rolls of the last cage.
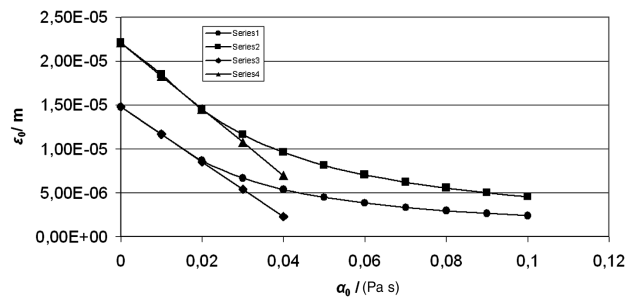
Figure 6: Effect of ε_a on ε_0^1 when $\alpha_0 \rightarrow 0$

Slika 6: Vpliv ε_a na ε_0^1 za $\alpha_0 \rightarrow 0$

Series/Serija 1 – $\varepsilon_a = 0.000\ 942$ m;
Series/Serija 2 – $\varepsilon_a = 0.0000\ 3141$ m;
Series/Serija 2 – $\varepsilon_a = 0.000\ 000\ 942$ m;
Series/Serija 4 – $\varepsilon_a = 0.000\ 003141$ m;
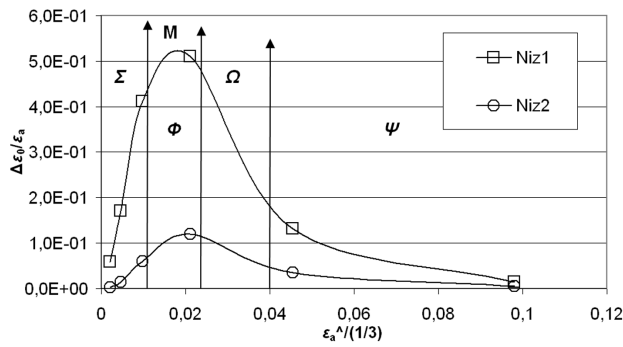Series/Serija 3 – $\varepsilon_a = 0.000\ 000\ 094205$ m

Figure 7: ε_a influence on deltas ε_0
Series 1, $(\varepsilon_0^1 - \varepsilon_0^{0.1})/\varepsilon_a; \varepsilon_0^{0.1}$ – lubricant height for the angle of engagement of 0.1 rad; Series 2, $(\varepsilon_0^1 - \varepsilon_0^*)/\varepsilon_a$
Slika 7: Vpliv ε_a na delta ε_0
Serija 1, $(\varepsilon_0^1 - \varepsilon_0^{0.1})/\varepsilon_a; \varepsilon_0^{0.1}$ – debelina maziva za orpijemni kot 0.1 rad; serija 2, $(\varepsilon_0^1 - \varepsilon_0^*)/\varepsilon_a$

The solutions of the differential Equation (3) in **Figures 5, 6, and 7** were obtained by applying the Monte-Carlo numerical method. We also tried to obtain approximate analytical solutions using the square polynomial in Equation (7). **Table 2** clearly shows this according to the marked areas in **Figure 7**.

Table 2: Approximate analytical solutions of the differential Equation (3) for the area of linearity.
Tabela 2: Aproksimativne analitične rešitve diferencialne enačbe (3) za področje linearnosti

Zone of Figure 7	Approximate analytical solution
Ψ	$\varepsilon_0^* = 0.7726\varepsilon_0^1 \quad \varepsilon_0^* = 0.5R_0(\alpha^*)^2 \quad \alpha^* = \sqrt[3]{\dfrac{8}{15R_0A}}$
Ω	$\alpha^* = 2\cdot\sqrt[3]{\dfrac{\varepsilon_a\sqrt{2R_0\varepsilon_a}}{10R_0^2+15R_0A\varepsilon_a\sqrt{2R_0\varepsilon_a}}} \quad \varepsilon_0^* = \dfrac{R_0(\alpha^*)^2}{2}$
M	$\alpha_0^* = \left(\dfrac{2}{5}\right)^2 \dfrac{1}{A\varepsilon_{aMAX}} \quad \varepsilon_0^* = \dfrac{R_0(\alpha_0^*)^2}{2} \quad \varepsilon_{aMAX} = 0.28674\cdot\sqrt[3]{\dfrac{R_0}{A^2}}$
Φ Σ	$\varepsilon_0^1 = \varepsilon_a\left(1-\dfrac{0.57348\varepsilon_a}{\varepsilon_{aMAX}}\right) \quad \varepsilon_{aMAX} = 0.28674\cdot\sqrt[3]{\dfrac{R_0}{A^2}}$

Note: indices (0 and *) refer to the discriminant of the trinomial of the second power in Equation (7) that limits to zero. The indices (0 and 1) are given for the case of $\alpha_0 \to 0$ rad.
ε_{aMAX} = height of the lubricant layer on the mandrel at the maximum in **Figure 7**.

The solution for the point M in **Table 2** can be used for the verification of numerical methods. The relations in the zone Ψ enable the linearity of the calculation presented in **Figure 5** and Series 3 and 4.

The comparison between the Monte-Carlo numerical method and the approximate analytical solutions in **Table 2** is given in **Table 3**. An acceptable matching of the results of both kinds of calculations is obtained. In a continuous rolling mill the stands before the inlet cross-section of the tube blank wall reduce the lubricant quantity, up to the point M, in a surplus over the quantity

Table 3: Comparison of Monte Carlo numerical method and analytical solutions in **Table 2** for the calculation of ε_0^*
Tabela 3: Primerjava numerične metode Monte Carlo in analitskih rešitev v **tabeli 2** za izračun ε_0^*

ε_a/m	Monte-Carlo ε_0^*/m	Zone Ω ε_0^*/m	Point M ε_0^*/m	Zone Φ, Σ ε_0^1/m
9.420E-04	1.225E-05	1.225E-05	-	-
8.735E-05	1.136E-05	1.129E-05	-	-
1.069E-05	5.801E-06	-	5.801E-06	-
7.425E-06	4.618E-06	-	-	4.466E-06
6.849E-06	4.373E-06	-	-	4.332E-06
1.210E-06	1.065E-06	-	-	1.081E-06
2.456E-07	2.362E-07	-	-	2.404E-07
1.205E-07	1.178E-07	-	-	1.192E-07
3.846E-08	3.809E-08	-	-	3.833E-08
1.046E-08	1.042E-08	-	-	1.045E-08
7.986E-09	7.962E-09	-	-	7.981E-09
4.123E-09	4.115E-09	-	-	4.121E-09
9.682E-09	9.676E-09	-	-	9.676E-09
3.141801E-10	3.1409E-10	-	-	3.1417E-10

that can be driven by the rolls into this zone. After ε_a entering the micro-area the opposite occurs, and wearing out of the lubrication takes place in the final stands of the continuous rolling mill. A similar effect is met during strip dressing, with the difference that the lubricant can be added before the rolls.

Table 3 presents filtered calculations according to the approximate analytical solutions in **Table 2**, obtained with a grapho-analytical approach. The domain of use for the zones Ω, Φ and Σ is determined by the common cross. It is necessary to point out that the Monte-Carlo numerical solution could also lead to conjugated-complex solutions for ε_0, and in the zones Φ and Σ. In this case it is necessary to increase Equation (7) with new members or start a new one with the original Equation (5). In areas where difficulties are found with the application of the numerical method, approximate analytical solutions are reliable. The solution for the lubricant abrasion on the mandrel in the last cages of the continuous rolling mill can be mastered with a proper geometrical relation of the mandrel and the working rolls. In new processes a graded mandrel is used to obtain more lubricant in the last cages of the rolling mill. A second geometrical solution for rolling with a mandrel with a constant section is based on the configuration of the rolls in the cages. A variant of this solution is shown in **Figures 3 and 4**.

4 CONCLUDING REMARKS

The effect of the lubricant-layer thickness ε_a on the lubricant-layer thickness on the rolling during the entering zone of the tube wall reduction ε_0 is analyzed for the longitudinal continuous rolling of seamless tubes using the long, floating mandrel. The calculation is made for the top of the rolling pass, which is in each subsequent cage turned by 90°. It can be considered that up

to point M in **Figure 7**, stable hydro-dynamical lubricating occurs. This means that the first and the second cages will be supplied with a surplus and the next cages with a shortage of lubricant. This shortage will be even greater in the last cages of finishing the tube with the final dimensions. In this position, the gripping angle for wall reduction approaches zero and ahead of the cage the quantity of lubricant is lower than that which could be driven in the deformation zone, and a shortage of lubricant is met. To overcome this problem the solution of Equation (2) was proposed in the graphical approach to a limit as the gripping angle approaches zero (by lowering the wall thickness Equation (2) approaches the mathematical definition for a limit). Equation (10) was developed for this case.

$$\varepsilon_0^1 = \varepsilon_a \left(1 - \frac{0.57348\varepsilon_a}{\varepsilon_{aMAX}}\right) \quad \varepsilon_{aMAX} = 0.28674 \cdot \sqrt[3]{\frac{R_0}{A^2}} \quad (10)$$

which is in acceptable agreement with the Monte-Carlo method.

The dependence in **Figure 7** allows us to make the following conclusions:

– with a small lubricant thickness on the mandrel (εa), in the zone of the wall deformation (ε_a); the effect of the process kinematics and of the lubricant rheology on the lubricant-layer thickness on the mandrel is greater than the effect of the rolling geometry;

– point M in **Table 2** makes it possible for us to calculate the lubricant-layer thickness at the initial state of the wall reduction, and this could be used to verify the transient Monte-Carlo solution for the same conditions;

– in the exit stands, when the lubricant-layer thickness on the mandrel (ε_a) approaches the boundary to the micro- and the nano-areas because the lubricant is worn out, the effect of the rolling geometry on the lubricant thickness in the deformation zone (ε_0) becomes stronger. The theoretical case of ε_a in the nano-area is analyzed and according to **Table 3** a good agreement was achieved with the Equations (10) and the numerical integration. This conclusion justifies the use of the graded mandrel in the rolling technology;

– for the theoretical analysis of the lubricant-layer thickness on the mandrel ahead of the zone of tube wall deformation, the solutions in **Table 2** are reduced to a triple point, which can be mathematically written according to relation (11).

$$\lim_{\substack{\varepsilon_a \to \varepsilon_0^1 \to \varepsilon_0^* \\ \alpha_0 \to 0}} \left[\text{equation (3)}\right] \to \left[\text{equation (10)}\right] \quad (11)$$

Thus, the solution of Equation (3) is the approach to the analytical relation (10). This is clear from **Figure 5**, where the increase in the dynamic viscosity cannot help to increase the lubricant-layer thickness in the zone of reduction of the wall thickness in the case when the lubricant-layer thickness on the mandrel (ε_a) decreases to the nano- range and the gripping angle for the tube approaches zero. Series 5 is calculated for the mandrel lubricant-layer thickness from 0 m to 0.000094205 m; it has a low angle to the abscissa (lubricant dynamical viscosity) and can be considered as constant for the average mandrel layer thickness and virtually independent of the zone of calculation in **Table 2**.

In this area the numerical Monte-Carlo method will give complex conjugated solutions. The approach has a synthetic irrational figure for the mandrel lubricant-layer thickness ahead of the point of the initial wall reduction on the basis of the irrational value of two ($\sqrt{2}$), which is included in ε_a.

5 REFERENCES

[1] I. Mamuzić, V. M. Drujan, Teorija, Materijali, Tehnologija, Čeličnih cijevi, Hrvatsko Metalurško Društvo, Zagreb 1996, 137–275

[2] S. V. Mazur, Postanovka zadači i zakonomernosti tečenija smazki v očage deformacii pri prokatke trub, Sučasni problemi metalurgii, 8 (**2005**), 447–452

[3] D. Ćurčija, I. Mamuzić, Mater. Tehnol., 39 (**2005**) 3, 61–77

[4] O. P. Maksimenko, A. A. Semenča, Issledovanie kontaktno-gidrodinamičeskoj smazki pri prokatke. Sučasni problemi metalurgii, 8 (**2005**), 99–103

[5] P. L. Klimenko, Kontaktniie naprjaženija pri prokatke s tehnologičeskoj smazkoj, Sučasni problemi metalurgii, 8 (**2005**), 44–49

[6] D. Ćurčija, Mater. Tehnol., 37 (**2003**) 5, 237–251

[7] D. Ćurčija, I. Mamuzić, Metalurgija 44 (**2005**) 3, 221–226

[8] D. Ćurčija, I. Mamuzić, Metalurgija 44 (**2005**) 4, 295–300

[9] D. Ćurčija, I. Mamuzić, Lubricating film shape at band dressing, 38 Symposium Lubricants, Društvo za Goriva i Maziva, Zagreb, Rovinj 19–21 10, 2005. Croatia (will by publisehed)

THE INFLUENCE OF COOLING RATE ON THE MICROSTRUCTURE OF AN Al-Mn-Be ALLOY

VPLIV OHLAJEVALNE HITROSTI NA MIKROSTRUKTURO ZLITINE Al-Mn-Be

Niko Rozman, Tonica Bončina, Ivan Anžel, Franc Zupanič

University of Maribor, Faculty of Mechanical Engineering, Smetanova 17, SI-2000 Maribor, Slovenia
niko.rozman@uni-mb.si

In ternary Al-Mn-Be alloys a metastable quasicrystalline phase can form at relatively low cooling rates ($\approx$ 100 K/s); however, besides the quasicrystalline phase other phases can also be present. We found that the investigated alloy is very prone to the formation of metastable phases, which are also quasicrystalline. Using different investigation methods we determined the type of phases, their shape, morphology, chemical composition and distribution. Special attention was given to the micro- and nano-sized quasicrystalline particles. When using slow cooling, $Al_{10}Mn_3$ and Be_4AlMn were present; however, with a faster cooling rate a quasicrystal approximant and a quasicrystalline phase were formed.

Key words: aluminium, quasicrystals, cooling rate, microstructure

V ternarnem zlitinskem sistemu Al-Mn-Be lahko nastane metastabilna kvazikristalna faza pri relativno majhni ohlajevalni hitrosti ($\approx$ 100 K/s), vendar lahko poleg nje nastanejo še druge kristalne faze (predvsem intermetalne faze). Z uporabo različnih raziskovalnih metod smo ugotovili vrsto nastalih faz, kemijsko sestavo in porazdelitev. Ugotovili smo, da je zlitina nagnjena k nastanku metastabilnih faz (tudi kvazikristalnih). Predvsem so zanimivi kvazikristalni delci, ki se pojavljajo v mikro- in nanometrskih velikostih. S počasnim ohlajanjem so nastale faze $Al_{10}Mn_3$ in Be_4AlMn, pri hitrem ohlajanju pa so se namesto njih pojavili kvazikristalni aproksimanti in kvazikristalne faze.

Ključne besede: aluminij, kvazikristali, ohlajevalna hitrost, mikrostruktura

1 INTRODUCTION

The production and application of aluminium alloys has increased considerably in the past few decades because of their good strength-to-weight ratios. Their use is justified in a variety of processes where a light and corrosion-resistant material is needed. The progress of aluminium alloys is leading to better mechanical properties and to improvements in the relatively poor strength and heat resistance of classical aluminium alloys [1].

The properties of an alloy depend on its chemical composition, structure and microstructure, which in turn depends on a variety of production conditions. Thermal treatment (quenching in our case) is one of the influences that affects the microstructure. In this research the effect of the solidification and cooling rates on the microstructure is investigated.

The alloy investigated was an Al-Mn-Be alloy, one of less-investigated alloys so far. Al-Mn alloys are suited for the manufacturing of metastable quasicrystalline materials with rapid solidification. In the past few years it was discovered by Song et al. [2] that the addition of beryllium to an Al-Mn alloy reduces the solubility of manganese in an aluminium solid solution and leads to the formation of quasicrystals and quasicrystal approximants at lower cooling rates. In practice, for the production of quasicrystals other aluminium based alloys are also used, for example, Al-Cu-Fe, Al-Cu-Cr, Al-Mn-B, Al-Cr-B, and Al-Si-Mn [2–5].

A quasicrystal is an intermediate state between a crystalline and an amorphous material. Quasicrystals normally have a non-characteristic symmetry and are not periodic; however, they do have long-range order (quasi-periodicity). It is usually more difficult to obtain the quasicrystalline state rather than the crystalline state, hence we do not know the conditions for quasicrystalline growth. We only have predictions based on their diffraction patterns. Quasicrystals can be stable or metastable. The metastable phases usually form from the melt with rapid cooling or large undercooling. Upon heating, these phases transform into stable crystalline phases. A survey of quasicrystals and their approximants can be found in reference [6].

In this study an Al-Mn-Be alloy was solidified with different cooling rates using melt spinning and casting into a special copper mould and cooling in a controlled manner (DSC analysis). The main aim of this work was to explore the influence of solidification and cooling rate on the microstructure.

2 EXPERIMENTAL

The Al-Mn-Be (M5) alloy was manufactured using the master alloys AlMn30 and AlBe5.5 and pure aluminium (Al 99.99 %). A charge was melted in a

LEYBOLD-HEREAUS IS vacuum furnace. The chemical composition of the M5 alloy is shown in **Table 1**. The relatively high content of Mn was selected in order to attain an appropriate volume fraction of quasi-crystalline phase in the rapidly solidified ribbons, whereas the large content of Be ensured the formation of the quasicrystalline phase with casting in a copper mould. Since it was a new alloy and therefore its properties were not known, we conducted a differential scanning calorimetry (DSC) analysis in order to determine the liquidus, solidus and other transformation temperatures. The DSC analysis was performed on apparatus from Bähr Thermoanalyse GmbH with heating and cooling rates of 10 °C/min. Since beryllium is highly reactive with air at high temperatures the DSC analysis was performed in an inert atmosphere.

Table 1: Chemical composition of the investigated alloy
Tabela 1: Kemijska sestava preiskovane zlitine

Alloy	Al $w/\%/x/\%$	Mn $w/\%/x/\%$	Be $w/\%/x/\%$
M5	90.6/86.1	5.4/2.5	4.0/11.4

$w/\%$ (mass fractions), $x/\%$ (mole fractions)

A specimen cooled at ≈ 1 °C/s was obtained by vacuum melting and casting into a 50 mm × 20 mm × 300 mm steel mould. It was then used as a reference material for determining the influence of quenching on the formation of the microstructure of the investigated alloy. A quenching rate of above 100 K/s was attained by casting into a special 10 mm × 1 mm × 100 mm copper mould. The largest cooling rate of between 10^5 K/s and 10^6 K/s was obtained by casting on a model M10 melt spinner (Marko Materials).

The metallographic investigation of alloys was carried out using light microscopy (LM) and scanning electron microscopy (SEM). The micro-chemical analysis was performed with energy-dispersive spectroscopy (EDS) and with Auger electron spectroscopy (AES); since beryllium could not be reliably detected with EDS most of the analyses were performed with AES. The AES analysis was performed with a high-resolution spectrometer with a field-emission MICROLAB 310F. The general characterisation of the phases was made with x-ray diffraction (XRD), and for the characterisation of very small particles, that could not be reliably analysed with XRD, transmission electron microscopy (TEM) was used.

3 RESULTS AND DISCUSSION

To investigate the formation of phases in the investigated alloy in conditions close to the equilibrium condition a DSC analysis was performed with a heating and cooling rate of 10 K/min, assuming that the temperature gradient was sufficiently small to achieve the transformations close to the thermodynamic equilibrium.

The DSC analysis showed the temperature of formation of the individual phase and the amount of energy absorbed or released in the process. Several transformations occurred during heating and cooling, and they are indicated in **Figure 1** (a and b). **Figure 1a** shows that the melting is completed at 945 °C, so it is obvious that we had to heat the alloy above this temperature before casting to achieve the melting of all the constituents of the alloy. On the cooling curve (**Figure 1b**) the peak 4 at 934 °C is probably connected with the formation of an oxide ($BeO\cdot AlO_2$) and does not indicate a solidus temperature of an alloy phase. Oxide particles may act as heterogeneous nucleation sites during the subsequent alloy solidification. The liquidus temperature at a cooling rate of 10 K/min was 870 °C and the solidus temperature of ≈ 640 °C depends on how the cooling rate affects the undercooling interval, which then affects the transformation temperatures. As shown in the **Figure 1c** applying XRD, SEM and EDS the
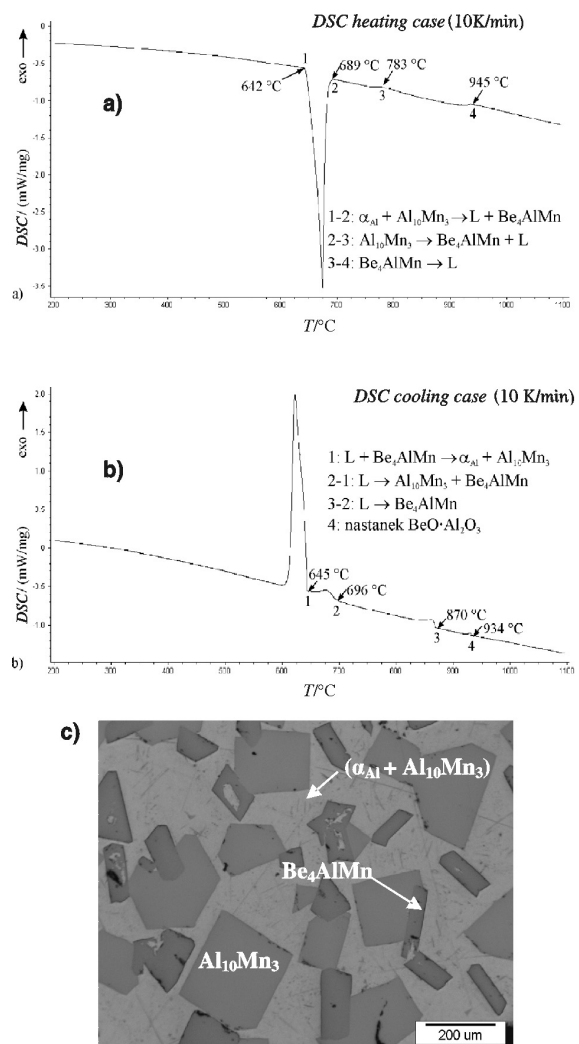

Figure 1: a) DSC analysis of heating, b) DSC analysis of cooling, c) microstructure after DSC cooling
Slika 1: a) DSC-analiza segrevanja, b) DSC-analiza ohlajanja, c) mikrostruktura

Table 2: Characteristics of the phases in the investigated Al-Mn-Be alloy
Tabela 2: Značilnosti faz v preiskani zlitini Al-Mn-Be

Casting Litje	Phases Faze	Size of phases Velikost faz	Chemical composition (x/%) Kemijska sestava (x/%)
Casting into steel mould Litje v jekleno kokilo	α_{AL} $Al_{10}Mn_3$ Be_4AlMn	up to 100 µm 10-20 µm	66 % Be, 7 % Mn, 20 % Al
Casting into copper mould Litje v bakreno kokilo	Rod-like eutectic (paličast evtektik)	–	–
	Hexagonal approximant (heksagonalni aproksimant)	1–2 µm	73 % Be, 7 % Mn, 20 % Al
	Quasicrystals (kvazikristali)	0.2–1 µm	30 % Be, 15 % Mn, 55 % Al
Melt spinning (wheel-side) Ohlajanje na vrtečem se kolesu (ob kolesu)	Quasicrystals (kvazikristali) α_{AL}	up to 50 nm	35 % Be, 15 % Mn, 50 % Al
Melt spinning (air-side) Ohlajanje na vrtečem se kolesu (na zunanji strani)	Quasicrystals (kvazikristali) α_{AL}	up to 500 nm	35 % Be, 15 % Mn, 50 % Al

phases $Al_{10}Mn_3$ and Be_4AlMn were identified in the eutectic ($\alpha + Al_{10}Mn_3$) matrix. The sizes of the phases are given in **Table 2**. It is interesting to note that stable phases from the ternary phase diagram like $Al_{15}Mn_3Be_2$ and Al_6Mn were not found [7]. This is not very unusual since in the binary Al-Mn system, as well as in the higher component systems based on this system, meta-stable phases very often form [7].

In **Figure 2** the microstructure obtained at an increasing cooling rate is shown. During relatively slow cooling with solidification in the steel mould (**Figure 2a**) the microstructure consists of $Al_{10}Mn_3$ phases, smaller faceted B_4AlMn phases and a eutectic matrix. These phases were of the same type as the phases formed during the DSC cooling. The size of the phases was smaller because of the greater cooling rate and the greater undercooling. After casting into the 1-mm copper mould the melt temperature was decreased faster and a larger undercooling was achieved. **Figure 2b** shows the corresponding microstructure with small, bright
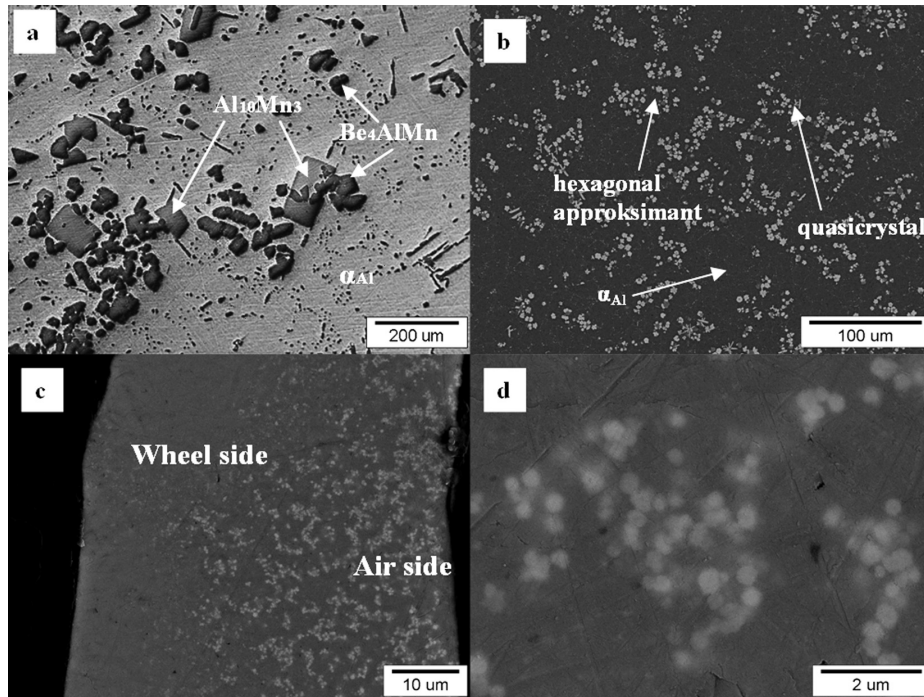

Figure 2: Microstructure of a) reference sample, b) sample casted in copper mould, c) melt-spun ribbon, d) microstructure of the air side of the ribbon
Slika 2: Mikrostruktura: a) referenčni vzorec, b) lit v bakreno kokilo, c) lit na vrteči se boben, d) leva stran traku

quasicrystal particles uniformly distributed in the Al-rich matrix. The size of these particles was significantly smaller than the size of the phases formed at a slower cooling rate (**Table 2**). With deep etching, scanning electron microscopy, x-ray diffraction and TEM we proved that these small particles did not belong to the same phases as those obtained with the slower cooling rates and were identified as hexagonal approximants and quasicrystals, as reported in reference [8]. The matrix consisted of a eutectic of a quasicrystalline phase (with a rod-like morphology) and the Al-rich solid solution α-Al.

The microstructure of a melt-spun ribbon with a thickness between 40 μm and 60 μm is shown in **Figure 2c**. Rapid solidification ($\approx 10^6$ K/s) produced a large undercooling, allowing the formation of only the quasicrystalline phase, present in the form of dispersed particles in an Al-rich matrix. The left-hand side of the ribbon was in contact with the wheel and the right-hand side with the atmosphere. With optical microscopy no particular phase was detected in the microstructure, while high-resolution SEM and TEM showed that the microstructure consisted of relatively uniformly distributed quasicrystalline particles of sizes around 50 nm. The cross-section of the ribbon shows the influence of the cooling rate on the particles and their size. Using a smaller cooling rate, i.e., at a larger distance from the wheel side of the ribbon the particle size was greater. According to the morphology, the quasicrystals were presumably formed in the melt before the solidification of the Al-rich matrix. On the wheel side, where the solid interface propagated with a faster rate, the quasi-crystalline particles were often entrapped in the matrix. On the air-side of the ribbon the solidification was slower. The morphology of α_{Al} was dendritic and the quasicrystalline particles were entrapped in the interdendritic space.

The chemical composition of the phases shown in **Table 2** was determined with EDS and AES. Under equilibrium conditions, according to the ternary phase diagram, the alloy M5 should contain many intermetallic phases. Intermetallic particles were present in the microstructure obtained with a slow solidification rate; however, they were not the same as those in the Al-Mn-Be equilibrium ternary phase diagram. Inter-metallic phases have a different crystallographic structure than the solid solutions and represent an independent sort of crystal with high hardness and low ductility [9].

Table 2 clearly shows that with an increasing cooling rate, not only does the size of the particles become smaller, but the type of phases changes also. According to the chemical composition the intermetallic phase $Be_{10}MnAl_3$ could be a hexagonal approximant.

4 CONCLUSIONS

The formation of phases in the investigated alloy depends on the cooling rate. It was confirmed that the investigated Al-Mn-Be alloy is prone to the formation of metastable phases. Using DSC the $Al_{10}Mn_3$ and Be_4AlMn phases were found to be present in the Al-rich matrix. A small increase in the cooling rate by casting into a steel mould did not lead to the formation of new phases, but only to smaller sized particles, apparently because of the reduction of coarsening in the faster-solidifying undercooled melt. The additional increase of cooling rate by casting into a small copper mould resulted in the creation of a hexagonal quasicrystalline approximant (a crystalline phase that closely resembles the quasicrystalline phase in terms of structure and properties). Finally, with the fastest cooling, produced by melt spinning, only quasicrystals formed in the α-Al solid solution.

Uniformly distributed quasicrystals and their approximants could act as dispersion-strengthening elements and improve the strength-to-weight ratio of the alloy.

5 REFERENCES

[1] Evans W J: Jom – A publication of the minerals, Metals & Materials Society (**2007**), 30–36

[2] Song G S, Fleurey E, Kim S H, Kim W T, Kim D H: J. Mater. Res. 17 (**2002**), 1671–1677

[3] Trambly de Laissardiere G, Nguyen-Manh D, Mayou D: Progres in Material Science 50 (**2005**), 679–788

[4] Holland-Moritz D, Lu I R, Wilde G, Schroers J, Grushko B: Journal of Non-Crystalline Solids 250–252 (**1999**), 829–832

[5] Fisher I R, Kramer M J, Islam Z, Wiener T A, Kracher A, Ross A R, Loggraso T A, Goldman A I, Canfield P C: Materials Science and Engineering 294–296 (**2000**), 10–16

[6] Kelton K F: Quasicrystals: structure and properties, International Materials Reviev, 38 (**1993**), 105–137

[7] Mondolfo L F: Aluminium alloys, structure and properties, London, Boston, Sydney, Wellington, Durban, Toronto, Butterworths-London 1976, Aluminium-beryllium-magnesium systems, 447–448

[8] Bončina T: Characterisation of quasicrystalline alloys – Master degree work, Faculty of natural sciences and engineering, University of Ljubljana, 2006 Ljubljana

[9] Spaić S: Fizikalna metalurgija; University of Ljubljana, Faculty of Natural Sciences and Engineering, 1996 Ljubljana

TAILORING THE MICROSTRUCTURE OF ZnO-BASED CERAMICS

KONTROLA RAZVOJA MIKROSTRUKTURE V ZnO KERAMIKI

Slavko Bernik, Matejka Podlogar, Nina Daneu, Aleksander Rečnik

Jožef Stefan Institute, Jamova cesta 39, 1000 Ljubljana, Slovenia
slavko.bernik@ijs.si

In polycrystalline materials – both metals and ceramics – understanding and controlling the microstructure is very important since vital physical properties, critical for applications, are strongly influenced by the average grain size, the grain size distribution and the porosity. The influence of the microstructure is very straightforward in the case of the exceptional current-voltage nonlinearity of ZnO-based varistor ceramics, which is closely related to the ZnO grain size: a coarse-grained microstructure results in a low breakdown voltage for the ceramics, while a fine-grained microstructure is required for a high breakdown voltage. The grain size in high-voltage varistor ceramics is controlled by the addition of a spinel-forming additive, typically Sb_2O_3. The grain-growth inhibition is due to the reduced grain-boundary mobility caused largely by the pinning effect of the spinel particles and defines the approach to the preparation of ZnO-based varistor ceramics, and hence also the composition. Spinel-forming dopants such as Sb_2O_3, TiO_2 and SnO_2 also result in the formation of inversion boundaries (IBs) in the ZnO grains. We have identified an IB-induced grain-growth mechanism and showed that it controls microstructure development, while the role of the spinel is subordinated. Fundamental research that revealed the true nature of the grain growth in varistor ceramics enabled us to take an entirely new approach to tailoring either a coarse- or fine-grained microstructure for ZnO-based ceramics, and will significantly alter the preparation of varistors for all voltage ranges.

Key words: ZnO, ceramics, microstructure, grain growth, inversion boundaries

V polikristaliničnih materialih – v kovinah in keramiki – sta razumevanje in kontrola mikrostrukture ključnega tehnološkega pomena, saj so bistvene fizikalne lastnosti za uporabo teh materialov močno odvisne od povprečne velikosti zrn, porazdelitve velikosti zrn in poroznosti. Vpliv mikrostrukture je morda najbolj neposredno izražen v primeru tokovno-napetostne nelinearnosti varistorske keramike na osnovi ZnO, ki so tesno povezane z velikostjo zrn ZnO; medtem ko grobo zrnata mikrostruktura vodi do nizke prebojne napetosti, je za keramiko z visoko prebojno napetostjo zahtevana drobnozrnata mikrostruktura. Za kontrolo velikost zrn v varistorski keramiki so dodani dopanti, ki z ZnO tvorijo spinelno fazo, navadno je to Sb_2O_3. Razumevanje zaviranja rasti zrn zaradi prisotnosti spinelne faze na mejah med zrni, kar zmanjša njihovo mobilnost, je močno vplivalo na način priprave varistorske keramike in s tem tudi na njeno sestavo. Dopanti, kot so Sb_2O_3, TiO_2 in SnO_2, ki povzročijo nastanek spinelne faze, sprožijo tudi nastanek inverznih mej (IBs) v zrnih ZnO. Identificirali smo mehanizem rasti zrn pod vplivom inverznih mej in pokazali, da le-to prvenstveno kontrolira razvoj mikrostrukture, medtem ko je vpliv spinelne faze obrobnega pomena. Osnovne raziskave, s katerimi smo pojasnili dejanske mehanizme rasti zrn v varistorski keramiki, so nam omogočile popolnoma nov način priprave bodisi grobo- ali drobnozrnate mikrostrukture keramike na osnovi ZnO, kar je izredno pomembno za pripravo varistorjev za različna napetostna področja.

Ključne besede: ZnO, keramika, mikrostruktura, rast zrn, inverzne meje

1 INTRODUCTION

In polycrystalline materials – both metals and ceramics – understanding and controlling the microstructure is very important since such vital properties as mechanical strength, electrical conductivity, magnetic susceptibility, optical transmission, etc., are strongly influenced by the average grain size, the grain size distribution and the porosity. The microstructure is a directly related to grain-growth mechanisms. Grain growth, one of the fundamental subjects in material science and processing, has been studied for more than 50 years.

The influence of grain size on the electrical characteristics of ceramics is perhaps most straightforward in the case of the exceptional current-voltage nonlinearity of ZnO-based varistor ceramics. Here, the breakdown voltage – the transition from a highly resistive to a highly conductive state – is a direct function of the grain size: a coarser grain size results in lower breakdown voltages, while for a higher breakdown voltages a finer grain size is required. ZnO-based varistor ceramics are obtained by the addition of small amounts of oxides of Bi, Sb, Ti, Co, Mn, Ni, Cr, Al and others to ZnO powder, and then sintering in air within the temperature range from 1100 °C to 1300 °C, typically at 1200 °C. The current-voltage nonlinearity of the varistors is a grain-boundary phenomenon with an ideal breakdown voltage of the grain boundary at about 3.2 V. As the breakdown voltage of a varistor is the sum of the breakdown voltages of all the non-linear (varistor) grain boundaries between the electrodes, it depends on the number of grain boundaries per unit volume of the varistor ceramic, which is inversely proportional to the ZnO grain size.[1-3] Consequently, control of the grain growth in the processing of varistor ceramics is essential for the successful application of varistors in over-voltage protection in a broad range, from a few volts up to several kilovolts. Processing varistor ceramics with varying breakdown voltages per unit thickness – low,

medium or high – makes it possible to produce varistors with suitable dimensions (thickness) for any required voltage.

The microstructure development and grain growth in ZnO ceramics have been intensively studied in the past and the main emphasis was given to those varistor dopants that significantly influence the grain growth: Bi_2O_3, which not only induces the non-linearity in ZnO ceramics but also introduces a liquid phase to the system, [4-7] and spinel-forming dopants, especially Sb_2O_3 [8-10], TiO_2 [11,12] and Al_2O_3 [13-16], which are added to control the ZnO grain size in varistor ceramics. Due to the addition of Bi_2O_3, sintering and grain growth in varistor ceramics take place in the presence of a liquid phase, and the amount of added Bi_2O_3 has a major influence. [4,5] According to Bradt and coworkers, [6,7] the rate-controlling mechanism for ZnO grain growth is the phase-boundary reaction of the solid ZnO grains and the Bi_2O_3-rich liquid phase, which enhances the grain growth for additions of Bi_2O_3 up to the mole fraction 0.5 %, while for larger additions of Bi_2O_3 the rate-controlling mechanism changes to one of diffusion through the layer of the Bi_2O_3-rich liquid phase and the grain growth is slowed. While Sb_2O_3 is a standard dopant in fine-grained high-voltage varistor ceramics, TiO_2 is added to coarse-grained varistor ceramics with a low breakdown voltage. The inhibition of grain growth in Sb_2O_3-doped [8-10] and also Al_2O_3-doped [13-15] samples is generally explained by the reduced mobility of the ZnO grain boundaries due to the pinning effect of the spinel grains at the ZnO grain boundaries. A microstructure similar to that of Sb_2O_3 is obtained with SnO_2-doped varistor ceramics.[17] Sb_2O_3, SnO_2 and TiO_2 form a spinel phase with ZnO, and they also trigger the formation of inversion boundaries (IBs) in the ZnO grains. In the Sb_2O_3- and SnO_2-doped samples the IBs are present in most of the ZnO grains [9,17], and in the TiO_2-doped samples IBs are present only in some, regularly exaggeratedly grown grains.[12,18] While the possible role of IBs in the grain-growth process of Sb_2O_3-doped samples was only briefly considered [9] until recent years, in TiO_2-doped ZnO ceramics the exaggerated growth of ZnO grains in connection with IBs was observed by Makovec et al.[12]

Based on studies of microstructure development in ZnO ceramics doped with Bi_2O_3 and SnO_2 we realized that inversion boundaries (IBs) have a major influence on the grain growth of ZnO, while the influence of the spinel phase is subordinate to the role of IBs.[19] Studies of the microstructure development at lower temperatures, where the grain-growth kinetics is still slow, revealed that grains with IBs overgrow all the normal grains without an IB in their surroundings until they prevail in the microstructure. Based on these results we proposed an inversion-boundary-induced grain-growth mechanism. At temperatures below those for the formation of the spinel phase, in the early stage of sintering, IBs

nucleate in some ZnO grains. ZnO grains with an IB, i.e., a nucleus, anisotropically and exaggeratedly grow in the direction of the adopted defect (IB) until they collide with each other, and finally prevail in the microstructure. Consequently, it should be possible to tailor the grain size of ZnO ceramics by controlling the number of nuclei. A coarse-grained microstructure would develop from a smaller number of nuclei as the grains could grow to a larger size before they collide with each other. In contrast, with a larger number, nuclei would collide with each other when they are still small, which would result in a fine-grained microstructure. In diffusion-doped ZnO, sintered under a slightly increased partial pressure of Sb_2O_3, we demonstrated that higher concentrations of Sb_2O_3 resulted in a fine-grained microstructure with the absence of the spinel phase, while at a low concentration of the dopant, grains several times larger than normal developed in the Sb_2O_3-poor region of the ZnO ceramic.[20] A coarse-grained microstructure was obtained for the first time in Sb_2O_3-doped ZnO ceramics. These results showed that the amount of IBs-triggering dopant (Sb_2O_3) influences the number of nuclei, which indeed results in either a coarse-grained microstructure for a small number of nuclei or a fine-grained ZnO ceramic for a larger number of nuclei formed in the early stage of sintering.

To understand the role of spinel-forming dopants on the formation of IBs, their atomic structure, chemistry and nucleation were analysed by Recnik et al. [21,22] They found that the IB plane consists of an Sb-rich monolayer that contains 1/3 of Sb^{5+} and 2/3 of Zn^{2+} octahedrally coordinated ions, giving an average oxidation state of +III for each available octahedral interstice in the boundary plane. A study of IB nucleation revealed two competing mechanisms that take place, depending on the oxidation state of the IB-forming dopant: (i) internal diffusion, and (ii) surface nucleation and growth. The first mechanism prevails for III+ dopants and is controlled by the Zn-vacancy diffusion, whereas the second mechanism holds for all IB-forming dopants (oxides of Sb, Sn and Ti) and is controlled by chemisorption of the dopants on Zn-deficient (0001) surfaces. In both cases the driving force for the inversion is the preservation of the local charge balance. The IB structure – a sort of stable two-dimensional surface compound – is thermodynamically more stable than the reactants alone (ZnO and the IBs-triggering dopant).[19,22] Due to the driving force for incorporating the IB-forming dopant into the IB, the growth of the host ZnO grain is dictated by the direction of the IB plane and, consequently, such a grain is preferred in terms of growth over the normal grains without IBs. The process is controlled by surface diffusion of the IBs-triggering dopant and its incorporation into the structure of the IB.[22] The anisotropic and exaggerated growth of grains with IBs (nuclei) is caused by a nucleation mechanism for the IBs [22,23] An under-

standing of this mechanism explained the preferential growth of ZnO grains with IBs over normal grains.

Diffusion doping with Sb_2O_3 demonstrated that the amount of IBs-triggering dopant indeed influenced, via the IBs-induced grain-growth mechanism, the microstructure development in ZnO ceramics: with a larger amount of Sb_2O_3 a fine-grained microstructure is obtained, while a smaller amount of Sb_2O_3 results in coarse-grained ceramics.[20] Our further studies were aimed at investigating the possibilities for tailoring the microstructure, via the IBs-induced grain-growth mechanism, of ZnO ceramics doped with varying amounts of IBs-triggering dopant (Sb_2O_3) in a more usual way. We studied the microstructure development in low Sb_2O_3-doped ZnO ceramics [24] and afterwards also in ZnO ceramics doped with Bi_2O_3 and Sb_2O_3.[25] Tailoring the microstructure in the basic varistor system of ZnO ceramics doped with Bi_2O_3 and Sb_2O_3 with the IBs-induced grain-growth mechanism would mean the same possibility also for fully doped ZnO-based varistor ceramics. While in Sb_2O_3-doped ZnO only the $Zn_7Sb_2O_{12}$ spinel phase is formed, the chemistry of the ZnO-Bi_2O_3-Sb_2O_3 system, which defines the reactions in the varistor ceramics (other varistor dopants incorporate into the phases of this system), is much more complex and is influenced by the Sb_2O_3/Bi_2O_3 ratio: at 600 °C the $Bi_3Zn_2Sb_3O_{14}$ pyrochlore phase is already formed and this decomposes into a Bi_2O_3-rich liquid phase and $Zn_7Sb_2O_{12}$ above 1000 °C. The $Zn_7Sb_2O_{12}$ phase is formed above 800 °C in a direct reaction with ZnO, only when $x(Sb_2O_3)/x(Bi_2O_3) > 1$, and the liquid phase is present in the system already at 740 °C only for $x(Sb_2O_3)/x(Bi_2O_3) > 1$, otherwise it appears in the system only after the decomposition of the pyrochlore phase at much higher temperatures.[2,3]

In this paper a review of previously reported results [24,25] about the influence of the amount of added Sb_2O_3 or Sb_2O_3 and Bi_2O_3 for different $x(Sb_2O_3)/x(Bi_2O_3)$-to-$x(ZnO)$ ratios on the grain growth and formation of IBs in ZnO ceramics prepared by a classical ceramic procedure is discussed. The resulting microstructures of the samples sintered at 1200 °C were analyzed in terms of the grain size and the fraction of grains containing IBs, related to the starting composition and the sintering time.

2 EXPERIMENTAL

ZnO powder, Pharma A (Grillo Zinkoxid GmbH, purity > 99.9 %), with a uniform distribution of spherical particles was used for the preparation of Sb_2O_3- and Bi_2O_3-doped samples. Stable solutions of Bi-nitrate and Sb-acetate were used to add Bi^{3+} and Sb^{3+} to the ZnO powder for appropriate doping with Bi_2O_3 and Sb_2O_3. All the samples were prepared with the addition of equal amounts of a solution to 20 g of ZnO; the amounts of Bi^{3+} and Sb^{3+} solutions required for a particular sample

composition were diluted to 20 mL with ethanol. The obtained ZnO slurry was homogenized in a polyethylene mill with zirconia balls for 1 h at 200 r/min. After homogenization the slurry was dried in a vacuum drier to obtain a powdered sample. Camphor was added to the powder mixture as a pressing aid, and pellets with a diameter of 10 mm and a thickness of 2 mm were pressed from the powder mixture with a pressure of 150 MPa. ZnO-Sb_2O_3 samples were prepared with additions of Sb^{3+} (1, 5, 25, 50, 100, 250 and 500) μg/g, which correspond to amounts of the mole fraction from 0.000033 % Sb_2O_3 to 0.016716 %. The samples were sintered in air at 1200 °C for (2, 10, 20, 50 and 250) h. The ZnO-Bi_2O_3-Sb_2O_3 samples were prepared with additions of the mole fraction 0.01 % Bi_2O_3, 0.02 % Bi_2O_3 and with equal additions of Bi_2O_3 for $x(Sb_2O_3)$-to-$x(Bi_2O_3)$ ratios of 0.8, 1.0 and 1.2. These samples were sintered in air at 1200 °C for 2 h and 10 h. To prevent any contamination among the samples with different compositions, each sample was placed into a separate, covered Al_2O_3 crucible. In addition, the sample pellets were placed between two pellets of the same composition, a bottom sacrificial one, to prevent contamination with the Al_2O_3 of the crucible, and a top one. The microstructure of each sample was prepared by grinding and polishing the sample pellet in a cross-sectional direction. Half of each microstructure was etched with dilute hydrochloric acid. The microstructures were analyzed on a scanning electron microscope (SEM) JEOL JSM-5800. Several SEM/BE images per sample were used for a stereological analysis of the ZnO grain size and the grain size distribution. The surface of each grain was measured and its size was calculated in terms of a diameter for circular geometry; the average ZnO grain size and the size distribution were determined from measurements of 400–1200 grains per sample. Details are given in references 24 and 25.

3 LOW Sb_2O_3-DOPED ZnO CERAMICS

The results of the ZnO grain-size analyses are summarized in **Table I** and graphically presented in **Figure 1**. The grain sizes of the ZnO samples doped with small amounts of Sb (Sb_2O_3) were strongly influenced by the amount of dopant and also by the sintering time. As expected, the ZnO grain size increased with longer sintering times; however, the increase in the grain size with time was very different with respect to the amount of added Sb. With the exception of the sample doped with 500 μg/g of Sb, all the other Sb-doped samples had a noticeably larger ZnO grain size – ranging from 26 μm to 32 μm – than the undoped ZnO (23 μm) after sintering for 20 h, which indicates a faster growth rate in the case of Sb-doped samples than in the case of pure ZnO. Longer sintering times resulted in a steady and more moderate increase in the ZnO grain size; in comparison to the undoped ZnO sample the

Table I: Results of the ZnO grain-size analysis of the ZnO samples doped with varying amounts of Sb and sintered at 1200 °C : average ZnO grain size G /μm with its standard deviation σ /μm and the fraction (in %) of the ZnO grains that contain an inversion boundary (IB).

Sample ZnO + y Sb y/(μg/g) (x(Sb$_2$O$_3$)/%)	1200 °C														
	2 h			10 h			20 h			50 h			250 h		
	G μm	σ μm	IBs %	G μm	σ μm	IBs %	G μm	σ μm	IBs %	G μm	σ μm	IBs %	G μm	σ μm	IBs %
0 (0)	**9.5**	4.3	0	**16.3**	7.6	0	**23.1**	9.8	0	**25.2**	10.5	0	**44.5**	19.4	0
1 (0.000033)	**11.4**	5.1	8	**19.6**	10.0	5	**26.1**	12.6	8	**29.3**	12.8	5	**56.2**	23.6	24
5 (0.000167)	**10.0**	4.9	10	**18.9**	9.2	15	**27.6**	11.6	20	**30.8**	14.1	10	**58.4**	25.4	31
25 (0.000835)	**9.2**	4.6	18	**20.2**	10.7	51	**32.3**	14.9	58	**43.4**	19.1	59	**71.3**	30.9	77
50 (0.001671)	**9.0**	4.6	24	**18.9**	9.7	56	**30.6**	13.0	62	**36.4**	16.2	63	**58.9**	24.6	77
100 (0.003342)	**9.9**	4.7	42	**18.7**	8.5	68	**27.4**	11.8	71	**30.3**	13.2	74	**54.0**	21.9	77
250 (0.008356)	**9.1**	4.8	43	**18.7**	8.9	70	**29.1**	13.3	72	**33.2**	15.5	73	**53.5**	22.4	78
500 (0.016716)	**3.4**	2.0	69	**8.5**	4.1	76	**9.7**	4.6	75	**10.0**	4.8	74	**11.9**	6.2	77

increase in the grain size was higher in the samples doped with (1, 5, 50 and 100) μg/g of Sb, being the highest in the sample doped with 25 μg/g of Sb, and similar in the sample doped with 250 μg/g of Sb. Consequently, the differences in ZnO grain size among the samples sintered for 20 h, and 50 h in the case of the sample with 25 μg/g Sb, remained either at the same level or increased even more after a longer sintering time. An exception was the sample with the addition of 500 μg/g of Sb, which has a lower growth rate than the other samples, even for sintering times shorter than 10 h, and especially for longer times. It has a much lower average ZnO grain size (about 10 mm) than all the other samples after 20 h of sintering, and the grain growth ceased so that further sintering for as long as 250 h
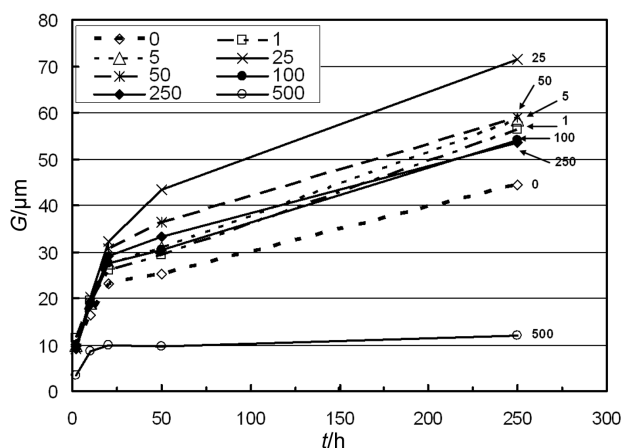
resulted in only a slight increase in the grain size, to about 12 μm.

Besides the differences in ZnO grain size, the fraction of ZnO grains that contains IBs is also different, depending on the amount of added Sb and the sintering time. The microstructures of the samples sintered for 10 h are presented in **Figure 2**. The results of the assessment of the fraction of ZnO grains with IBs in the samples with different amounts of Sb added to ZnO after different times at the sintering temperature are given in Table I and graphically presented in **Figure 3**. Both parameters, the amount of Sb and the sintering time, are dependent on each other and strongly influence the fraction of ZnO grains with IBs. In general, the fraction is higher in the samples with larger additions of Sb, it increases with the increasing time of sintering, and the grains with IBs develop in the microstructures after a shorter sintering time when the amount of added Sb in the sample is greater. However, in the ZnO sample doped with 500 μg/g of Sb the ZnO grains with IBs prevail (70 %) in the microstructure after 2 h of sintering, and after 10 h of sintering the grains with IBs completely dominate the microstructure.

The doping of ZnO with Sb resulted in coarse-grained microstructures for the samples with an average ZnO grain size noticeably larger than in the sample of undoped ZnO after sintering at 1200 °C. The only exception in this study was the sample with the largest amount of Sb added to the ZnO, 500 μg/g, which was fine-grained after prolonged sintering. These results contradict the standard understanding of the grain growth and microstructure development, i. e., that Sb$_2$O$_3$ doping results only in the inhibition of ZnO grain growth by the formation of spinel grains at the grain boundaries to reduce the grain mobility by the so-called Zener
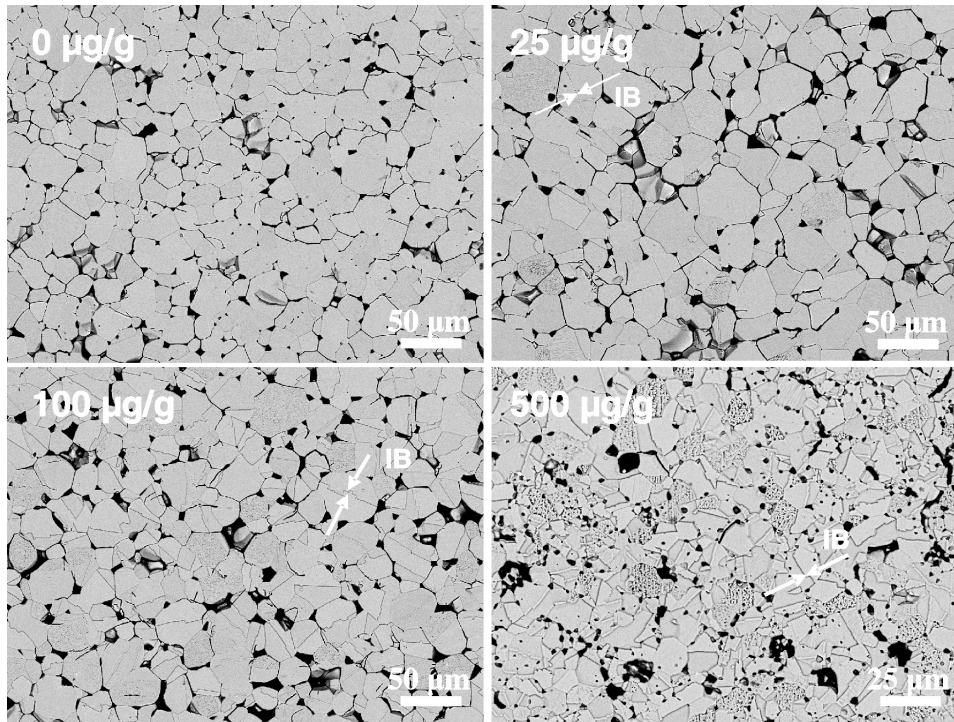

Figure 1: Average size of ZnO grain vs. sintering time at 1200 °C for samples with a varying amount of added Sb to the ZnO
Slika 1: Povprečna velikost zrn ZnO v odvisnosti od časa sintranja pri 1200 °C za vzorce z različnim dodatkom Sb v ZnO

Figure 2: Microstructures of un-doped ZnO sample and ZnO samples doped with (25, 100 and 500) µg/g Sb, sintered for 10 h at 1200 °C
Slika 2: Mikrostrukture nedopiranih vzorcev ZnO in vzorcev ZnO dopiranih s (25, 100 in 500) µg/g Sb, ki so bili sintrani 100 h pri 1200 °C

pinning effect. The actual microstructure development can be explained by an IBs-induced grain-growth mechanism,[19] and this is in agreement with other grain-growth studies.[20]

In this study it was observed that even the addition of just 1 µg/g of Sb to the ZnO results in the formation of IBs in some ZnO grains. With larger additions of Sb increasingly larger numbers of ZnO grains contain IBs, even after sintering for 2 h, and their fraction increases with longer sintering times. Consequently, ZnO grains with IBs dominate in the microstructures of the samples with the larger additions of Sb after shorter sintering times. In the sample with 500 µg/g of Sb, as many as 70 % of the ZnO grains contain an IB after 2 h of sintering, which showed that for a sufficient addition of Sb, grains with an IB completely dominate in the microstructure of the sample after a relatively short sintering time. The increase in the fraction of ZnO grains containing IBs with the sintering time is accompanied by an increase in the average grain size. A larger increase in the grain size with sintering time in Sb-doped samples in comparison to pure undoped ZnO can, therefore, be attributed to the presence of IBs in the ZnO grains. ZnO grains with IBs (nuclei) exhibit an enhanced grain growth when compared to normal grains; they grow at the expense of the normal grains, while their fraction increases and after a certain time of sintering, ZnO grains with IBs completely prevail in the microstructure.

After a short sintering time, most of the samples have a similar ZnO grain size. However, once the influence of the preferred growth of grains containing IBs starts to dominate in the microstructure, with a longer sintering time, the differences in the grain sizes among the samples become evident. Consequently, the grain sizes of the samples doped with Sb become larger than in the un-doped ZnO sample and the Sb-doped samples start to differ in terms of the ZnO grain size. The exception was the single sample with the largest addition of Sb, 500 µg/g, which is fine grained even after sintering for 250 h. In the 500 µg/g Sb sample the ZnO grains with IBs dominate in the microstructure even after a short
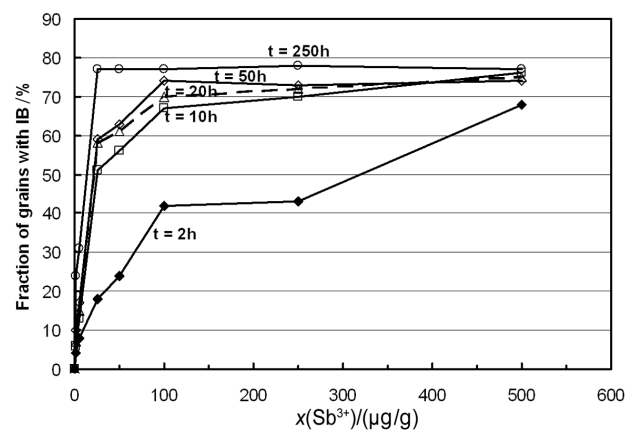

Figure 3: Fraction of ZnO grains with inversion boundaries (IBs) versus the amount of added Sb to ZnO for various sintering times
Slika 3: Delež ZnO zrn z inverznimi mejami (IBs) v odvisnosti od dodatka Sb v ZnO za različne čase sintranja

sintering time of 2 h, hence, their fraction and consequently also their grain size increased very little with an extended sintering time compared to other Sb-doped samples. The results indicated that with an increased amount of added Sb more ZnO grains contain IBs in the early stage of sintering, which determines the subsequent course of the grain growth and the final microstructure development. ZnO grains with IBs consume normal ZnO grains during their growth, and with their increasing fraction in the microstructure, the average ZnO grain size of the sample increases until the stage at which the grains with IBs completely dominate in the microstructure.

The longer is the period in which ZnO grains with IBs can grow at the expense of normal ZnO grains before they impinge upon each other, the larger they can grow and the coarser is the microstructure. In the sample with the addition of 25 µg/g of Sb, just the appropriate number of ZnO grains with IBs was formed in the early stage of sintering to take them a longer sintering time to prevail in the microstructure than in other Sb-doped samples, so the ZnO grains with IBs can grow larger than in any other sample. With the addition of 50 µg/g of Sb there was a slightly larger fraction of ZnO grains with IBs after sintering for just 2 h, which meant that the sintering time for their growth before they finally impinge on each other was somehow shorter and they are smaller after 20 and especially after 250 h (58 µm) than in the sample with 25 µg/g of Sb (71 µm). This is even more pronounced in the case of samples with 100 µg/g and 200 µg/g of Sb. The sample with the addition of 500 µg/g of Sb has a significantly smaller grain size of about 12 µm than all the other samples after sintering for 250 h. In this sample the ZnO grains with IBs prevail in the microstructure after sintering for 2 h.

From the graph of grain size vs. sintering time in **Figure 1** three regimes of noticeably different growth rates are evident: (i) an enhanced grain growth for sintering times up to 20 h, (ii) a modest growth rate for sintering times longer than 20 h and (iii) a grain growth that is practically terminated after 20 h of sintering. In the pure ZnO sample the grain growth is controlled by the solid-state diffusion of Zn^{2+} ions and follows Oswald-ripening growth kinetics. As long as the driving force for the reduction of a specific surface and hence the surface energy is sufficient, the grain growth is enhanced. However, as the average ZnO grain size of the sample noticeably increased after a longer sintering time, the driving force for grain growth decreased and the grain size increased modestly for sintering times longer than 20 h. In the Sb-doped samples, however, the regimes of the grain growth are related to the presence of IBs in the ZnO grains. In "regime I" ZnO grains with IBs coexist with normal ZnO grains. Because of the preferential growth of ZnO grains with IBs at the expense of normal grains, the grain growth is enhanced until ZnO grains with IBs dominate the microstructure.

The amount of added IB-forming dopant directly influences the number of grains with IBs, which develop in the early stage of sintering, and hence, also the time span of the grain-growth "regime I" in which the grains with IBs can grow at the expense of the normal grains. The longer is the duration of "regime I" of the microstructural development, the larger can grow the grains with IBs before they impinge on each other, and the coarser is the final microstructure of the sample. Once ZnO grains with IBs impinge on each other "regime II" of the grain growth starts and the grain growth is noticeably slowed. With large enough additions of Sb to make "regime I" short, resulting in a very fine-grained microstructure, and followed by "regime II", one observes "regime III" in which the ZnO grains practically do not grow any more and the Sb-doped ZnO ceramics remain fine grained, even after an extended sintering time. In this study that condition was observed only with the sample doped with 500 µg/g of Sb, which resulted in the nucleation of IBs in almost every ZnO grain so that they were in very close proximity of each other, even at the very beginning of the grain-growth process, and had a very small number of normal grains available for recrystallisation. Also, the addition of Sb to the 500 µg/g Sb sample was sufficient for the formation of the $Zn_7Sb_2O_{12}$ spinel phase.

The results fully confirmed the possibility of controlling the grain growth and microstructure development via an IBs-induced grain-growth mechanism with the amount of IBs-triggering dopant (Sb_2O_3) in ZnO ceramics prepared by a classic ceramic procedure. However, it also showed that a reduced number of ZnO grains infected with IBs in the early stage of sintering, depending on the amount of added Sb – lower for smaller and higher for larger additions of Sb – results only in a very narrow compositional range of added Sb_2O_3. Only within this range of amount of Sb_2O_3 added to ZnO can the grain size be varied from coarse to fine grained. With a larger amount of added Sb_2O_3 practically all the ZnO grains are infected with IBs in the early stage of sintering and the resulting final microstructure is fine grained. A detailed presentation and discussion of these results are given in ref. 24.

4 Bi$_2$O$_3$- AND Sb$_2$O$_3$-DOPED ZnO CERAMICS

The results of the ZnO grain-size analysis confirmed the uniform grain growth in the un-doped ZnO samples from the observation of the microstructure (**Figure 4**). In contrast, the addition of the mole fraction 0.01 % and 0.02 % of Bi_2O_3 to ZnO resulted in the exaggerated growth of some ZnO grains, while others remained fine grained, with a size in the range from below 1 µm to a few micrometers (**Figure 4**). The result of the grain-size measurements indicates a moderate, average ZnO grain size of about 11 µm for the Bi_2O_3-doped samples; however, the microstructures of these samples are
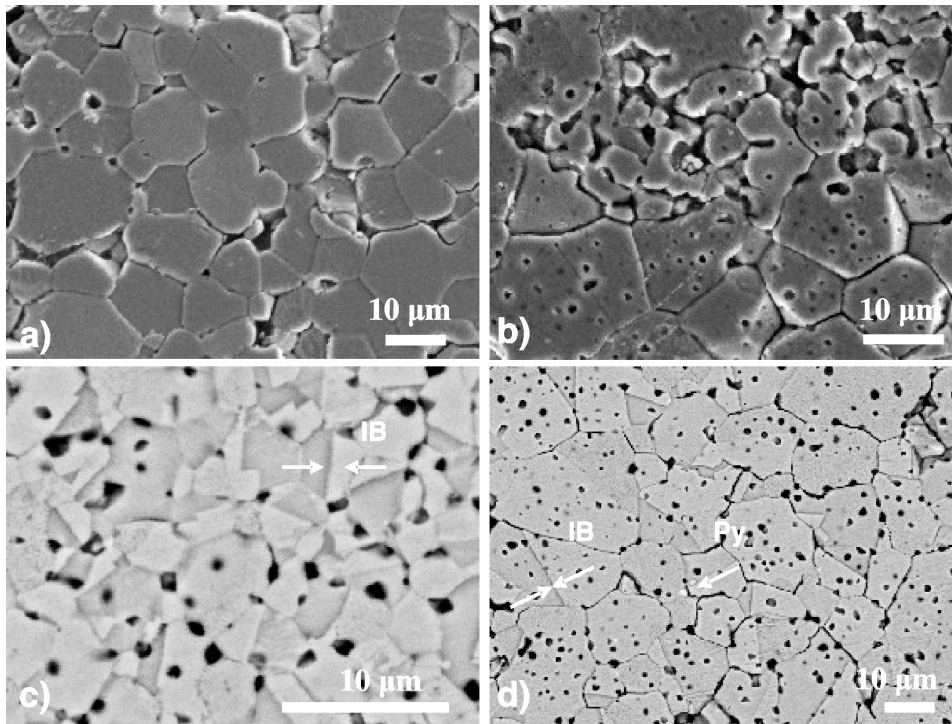
Figure 4: Microstructures of the samples sintered at 1200 °C for 2 h. a) ZnO; b) ZnO + 0.02 % Bi_2O_3; c) ZnO + 0.01 % Bi_2O_3 + 0.008 % Sb_2O_3; d) ZnO + 0.02 % Bi_2O_3 + 0.016 % Sb_2O_3. IB: inversion boundary; Py: pyrochlore phase; Bi_2O_3, Sb_2O_3 in mole fractions
Slika 4: Mikrostrukture vzorcev sintranih 2 uri pri 1200 °C. a) ZnO; b) ZnO + 0.02 % Bi_2O_3; c) ZnO + 0.01 % Bi_2O_3 + 0.008 % Sb_2O_3; d) ZnO + 0.02 % Bi_2O_3 + 0.016 % Sb_2O_3. IB: inverzna meja; Py: piroklorna faza; Bi_2O_3, Sb_2O_3 v molskih deležih
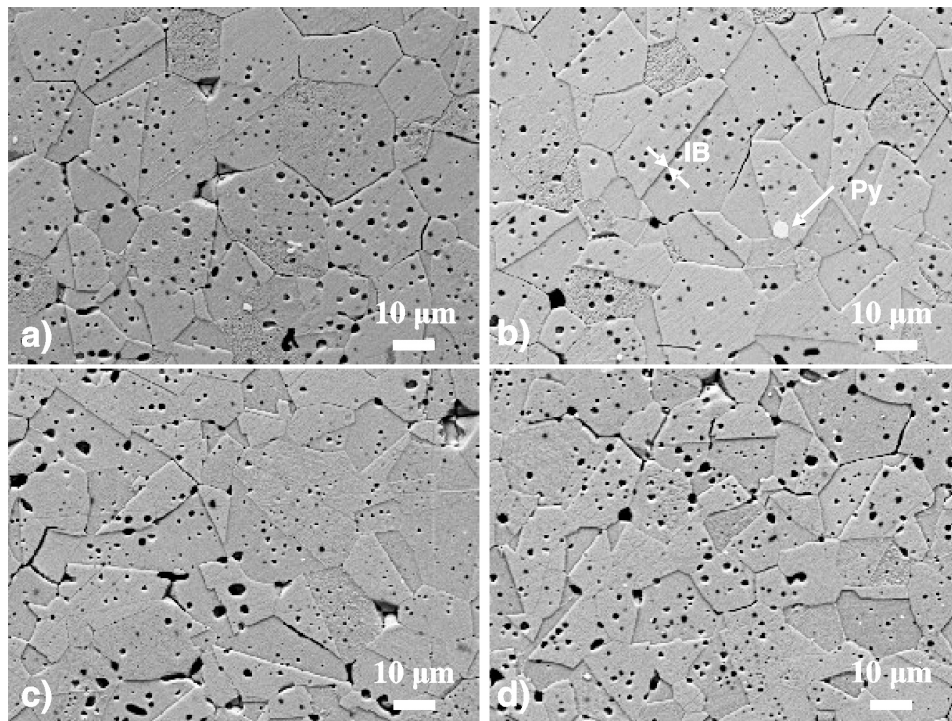
Figure 5: Microstructures of the samples sintered at 1200 °C for 10 h. a) ZnO + 0.01 % Bi_2O_3 + 0.008 % Sb_2O_3; b) ZnO + 0.02 % Bi_2O_3 + 0.016 % Sb_2O_3; c) ZnO + 0.01 % Bi_2O_3 + 0.012 % Sb_2O_3; d) ZnO + 0.02 % Bi_2O_3 + 0.024 % Sb_2O_3. IB: inversion boundary; Py: pyrochlore phase; Bi_2O_3, Sb_2O_3 in mole fractions
Slika 5: Mikrostrukture vzorcev sintranih 10 ur pri 1200 °C. a) ZnO + 0.01% Bi_2O_3 + 0.008 % Sb_2O_3; b) ZnO + 0.02 % Bi_2O_3 + 0.016 % Sb_2O_3; c) ZnO + 0.01 % Bi_2O_3 + 0.012 % Sb_2O_3; d) ZnO + 0.02 % Bi_2O_3 + 0.024 % Sb_2O_3. IB: inverzna meja; Py: piroklorna faza; Bi_2O_3, Sb_2O_3 v molskih deležih

actually highly bimodal and consist of very large ZnO grains surrounded by fine grains. In the sample with the mole fraction of 0.01 % Bi_2O_3 the largest grains have a size of about 60 μm, while in the sample with the mole fraction of 0.02 % Bi_2O_3 the largest grains are about 30 μm. At the grain boundaries of some grains a sufficient amount of Bi_2O_3-based liquid phase is present to ensure the exaggerated growth of these grains, while at the other boundaries the grain growth is hindered due to a lack of liquid phase.

The microstructures of the ZnO-Bi_2O_3 samples doped with Sb_2O_3 are shown in **Figures 4 and 5**. These results show that the addition of Sb_2O_3 strongly affects the microstructure development and the grain growth of ZnO doped with Bi_2O_3. In the reaction of Bi_2O_3 and Sb_2O_3 with ZnO the pyrochlore phase is formed, and its fine inclusions can be observed in the microstructures. Inversion boundaries (IBs) are clearly evident in most of the ZnO grains of Sb_2O_3-doped samples, regardless of the sintering time at 1200 μC. In comparison to the ZnO-Bi_2O_3 samples with exaggerated grain growth, the introduction of Sb_2O_3 resulted in a uniform grain growth. Samples with the addition of the mole fraction 0.01 % Bi_2O_3 and sintered for 2 h are fine grained with a grain size of about 2 μm for all Sb_2O_3/Bi_2O_3 ratios, while samples doped with the mole fraction of 0.02 % have an average ZnO grain size of about 6 μm, which is comparable to the un-doped ZnO, except the sample with a Sb_2O_3/Bi_2O_3 ratio of 1, which is fine grained. After sintering for 10 h most of the Sb_2O_3 doped samples have a similar ZnO grain size of about 10 μm, which is comparable to the grain size of the pure ZnO sample (12 μm), except for samples with a Sb_2O_3/Bi_2O_3 ratio of 1, which have a smaller grain size, especially the sample with the addition of the mole fraction 0.01 % Bi_2O_3; this sample remained fine-grained (2.8 μm).

The results of the microstructure analysis for the ZnO ceramics doped with small amounts of Sb_2O_3 and Bi_2O_3 indicated the complex influence of several factors on the grain growth: the amount of added Bi_2O_3, the formation of the pyrochlore phase, the Sb_2O_3/Bi_2O_3 ratio and the inversion boundaries (IBs) in the ZnO grains. The amount of added Bi_2O_3 defines the amount of liquid phase at the sintering temperature, while the amount of added Sb_2O_3 affects the nucleation of IBs in ZnO grains at the early stage of sintering and hence, the number of grains infected by IBs that can grow exaggeratedly. The formation of the pyrochlore phase bounds both the Bi_2O_3 and Sb_2O_3 at a very low temperature of about 600 °C, and hence affects their presence at temperatures below its decomposition at 1040 °C. In ZnO samples doped with such a small amount of Bi_2O_3, exaggerated grain growth occurs. The addition of Sb_2O_3 to ZnO doped with Bi_2O_3 results in uniform grain growth and the occurrence of inversion boundaries (IBs) in most of the ZnO grains. Grain growth is promoted by a sufficient amount of the Bi_2O_3 liquid phase at the grain boundaries and also the

presence of IBs in the ZnO grains. With a large enough addition of Bi_2O_3 the grain growth of ZnO grains with IBs is additionally promoted by the liquid phase and the grain size of the samples with a Sb_2O_3/Bi_2O_3 ratio smaller or larger than 1 is comparable to the grain size of the undoped ZnO samples. In the absence of a sufficient amount of the Bi_2O_3 liquid phase, the ZnO grains with IBs grow at a slower rate; however, after a longer sintering time the grain sizes of the samples with a Sb_2O_3/Bi_2O_3 ratio smaller or larger than 1 are comparable to the pure ZnO sample. The influence of the $Bi_3Zn_2Sb_3O_{14}$ pyrochlore phase formation is especially evident in the case of samples with a Sb_2O_3/Bi_2O_3 ratio of 1, where neither free Bi_2O_3 nor free Sb_2O_3 is present at temperatures below the decomposition of the pyrochlore phase, which consequently have a smaller ZnO grain size than the other samples.

5 CONCLUSIONS

The results fully confirmed the IBs-induced grain-growth mechanism and the possibility to use it for tailoring the microstructure in conventionally prepared ZnO ceramics doped with Bi_2O_3 and Sb_2O_3. For ZnO ceramics doped with Sb_2O_3, either a coarse-grained microstructure or a fine-grained microstructure, in comparison to pure ZnO, was obtained. Such results can be explained by the influence of IBs on the grain growth. The results showed that only very small amounts of Sb_2O_3, within a very narrow compositional range, result in a reduced number of ZnO grains infected with IBs (nuclei), so: i) for smaller amounts of Sb_2O_3, fewer nuclei are formed, which means they can grow for longer at the expense of normal ZnO grains before they impinge on each other and prevail in the microstructure, which results in a larger average ZnO grain size; and ii) for larger additions of Sb_2O_3, more nuclei are formed, which can grow to a lesser extent at the expense of normal ZnO grains before they impinge on each other and the final grain size is smaller. However, larger additions of Sb_2O_3 are sufficient to trigger the formation of IBs in most of the ZnO grains during the early stage of sintering and the resulting microstructure is fine-grained. In ZnO ceramics doped with Bi_2O_3 and Sb_2O_3 the complex influence of several factors on the grain growth is present: the amount of added Bi_2O_3, the formation of the $Bi_3Zn_2Sb_3O_{14}$ pyrochlore phase, and the Sb_2O_3-to-Bi_2O_3 ratio. They influence the amount of Bi_2O_3-rich liquid phase at the grain boundaries and also the presence of IBs in the ZnO grains, which strongly influence the grain-growth process. The results of these and previous investigations give us a comprehensive understanding of grain growth in ZnO ceramics under the influence of IBs; this enabled us to prepare ZnO ceramics doped with Bi_2O_3 and Sb_2O_3 with an average ZnO grain size that is either much larger or finer than for undoped ZnO ceramics.

6 REFERENCES

[1] D. R. Clarke, *J. Am. Ceram. Soc.*, 82 (**1999**), 485–502

[2] T. K. Gupta, *J. Am. Ceram. Soc.*, 73 (**1990**), 1817–1840

[3] M. Inada, *Jpn. J. Appl. Phys.*, 19 (**1980**). 409–419

[4] J. Kim, T. Kimura, T. Yamaguchi, *J. Am. Ceram. Soc.*, 72 (**1989**), 1541–1544

[5] J. Wong, *J. Appl. Phys.*, 51 (**1980**), 4453–4459

[6] T. Senda, R.C. Bradt, *J. Am. Ceram. Soc.*, 73 (**1990**), 106–114

[7] D. Dey, R. C. Bradt, *J. Am. Ceram. Soc.*, 75 (**1992**), 2529–2534

[8] J. Kim, T. Kimura, T.Yamaguchi, *J. Mater. Sci.*, 24 (**1989**), 2581–2586

[9] T. Senda, R.C. Bradt, *J. Am. Ceram. Soc.*, 74 (**1991**), 1296–1302

[10] M. Ito, M.Tanahasmi, M.Uehara, and A.Iga, *Jpn. J. Appl. Phys.*, 36 (**1997**), L1460–L1463

[11] H. Suzuki, R.C. Bradt, *J. Am. Cer. Soc.*, 78 (**1995**), 1354–1360

[12] D. Makovec, D. Kolar, M. Trontelj, *Mater. Res. Bull.*, 28 (**1993**), 803–811

[13] S. I. Nunes, R. C. Bradt, *J. Am. Ceram. Soc.*, 78 (**1995**), 2469–2475

[14] J. Han, P. Q. Mantas, A. M. R. Senos, *J. Mater. Res.*, 16 (**2001**), 459–468

[15] M. Tanahashi, M. Ito, M. Murao, A. Iga, *Jpn. J. Appl. Phys.*, 36 (**1997**), L573–L576

[16] S. Bernik, N. Daneu, *J. Europ. Ceram. Soc.*, 27 (**2007**), 3161–3170

[17] S. Bernik, N. Daneu, *J. Europ. Ceram. Soc.*, 21 (**2001**), 1879–1882

[18] S. Bernik, N. Daneu, A. Rečnik, *J. Europ. Ceram. Soc.*, 24 (**2004**), 3703–3708

[19] N. Daneu, A.Recnik, S. Bernik, and D. Kolar, *J. Am. Ceram. Soc.*, 83 (**2000**), 3165–3171

[20] N. Daneu, A. Rečnik, S. Bernik:, *J. Amer. Ceram. Soc.*, 86 (**2003**), 1379–1384

[21] A. Rečnik, N. Daneu, T. Walter, W. Mader, *J. Am. Ceram. Soc.*, 84 (**2001**), 2657–2668

[22] A. Rečnik. N. Daneu, S. Bernik, *J. Europ. Ceram. Soc.*, 27 (**2007**), 1999–2008

[23] A. Rečnik, M. Čeh. D. Kolar, *J. Europ. Ceram. Soc.*, 21 (**2001**), 2117–2121

[24] S. Bernik, J. Bernard, N. Daneu, A. Rečnik, *J. Am. Ceram. Soc.,* 90 (**2007**), 3239–3242

[25] S. Bernik, M. Podlogar, N. Daneu, A. Rečnik, *Mat. Sci. Forum,* 558–559 (**2007**), 857–862

A MECHANISM FOR THE ADSORPTION OF CARBOXYLIC ACIDS ONTO THE SURFACE OF MAGNETIC NANOPARTICLES

MEHANIZEM ADSORBCIJE KARBOKSILNIH KISLIN NA POVRŠINO MAGNETNIH NANODELCEV

Ana Drmota[1], Aljoša Košak[2], Andrej Žnidaršič[1,2]

[1]Kolektor Nanotesla Institute, Stegne 29, 1000 Ljubljana, Slovenia
[2] Kolektor Magma, d. o. o., Stegne 29, 1000 Ljubljana, Slovenia
ana.drmota@kolektor.si

The unique properties of magnetic nanoparticles, which are dominated by superparamagnetism, and the size dependence of those properties have led to a number of technological and biomedical applications of these materials and to the preparation of stable magnetic fluids or ferrofluids. The main problem relating to the stability of ferrofluids is the difficulty in controlling the dispersion of magnetic nanoparticles inside a liquid medium. To overcome this problem, functionalization of the nanoparticle surface is required. The efficiency of the functionalization process depends on the adsorption mechanism, which involves interactions of the surface-active agent molecules with the nanoparticle surface. The adsorption mechanism for oleic acid onto the surface of maghemite (γ-Fe$_2$O$_3$) nanoparticles prepared with the classic coprecipitation method was followed in solution using *in-situ* infrared spectroscopy (*React*IR). The synthesized maghemite nanoparticles were characterized using transmission electron microscopy (TEM), X-ray diffractometry (XRD) and specific surface area measurements (BET). The specific magnetization of the prepared samples was measured at room temperature with a DSM-10 magneto-susceptometer.

Key words: nanoparticles, precipitation, adsorption, infrared spectroscopy, surface active agent, carboxylic acid

Zaradi edinstvenih lastnosti magnetnih nanodelcev, ki izvirajo iz njihove superparamagnetne narave in so odvisni od velikosti nanodelcev, so magnetni nanomateriali zanimivi za vrsto tehnoloških in biomedicinskih aplikacij ter pri pripravi stabilnih magnetnih tekočin. Za doseganje stabilnosti magnetnih tekočin je potrebno magnetne nanodelce v nosilni tekočini površinsko funkcionalizirati. Učinkovitost procesa funkcionalizacije je odvisna od adsorpcijskega mehanizma, le-ta pa od interakcij med površinsko aktivno snovjo in površino nanodelca. Mehanizem adsorpcije oleinske kisline na površino maghemitnih (γ-Fe$_2$O$_3$) nanodelcev, ki smo jih pripravili z metodo koprecipitacije, smo spremljali v raztopini z uporabo *in-situ* infrardeče spektroskopije (*React*IR). Sintetizirane magnetne nanodelce smo karakterizirali z uporabo presevnega elektronskega mikroskopa (TEM), rentgenske praškovne difrakcije (XRD) in merjenjem specifične površine (BET). Specifično magnetizacijo (magneto-susceptometer, DSM-10) v odvisnosti od magnetnega polja smo merili pri sobni temperaturi.

Ključne besede: nanodelci, obarjanje, adsorpcija, infrardeča spektroskopija, površinsko aktivna snov, karboksilna kislina

1 INTRODUCTION

Magnetic nanoparticles are of great fundamental and technological interest because of their unique magnetic properties, which are dominated by superparamagnetism [1]. Magnetite (Fe$_3$O$_4$) and maghemite (γ-Fe$_2$O$_3$) nanoparticles represent the most often used magnetic materials due to their great potential in current and future technological and biomedical applications [2].

Numerous applications require the magnetic nanoparticles to be well dispersed in a liquid media, chemically stable and uniform in size. For this reason, many studies have focused on the preparation of magnetic fluids or ferrofluids, which represent a stable colloidal suspension of superparamagnetic nanoparticles with a narrow particle size distribution of around 10 nm, coated with a thin layer of surfactant molecules and stably dispersed in a polar or non-polar carrier liquid.

According to the type of carrier liquid, two main groups of ferrofluids are distinguished: *ionic aqueous-based ferrofluids*, if the nanoparticle surface is electrically charged, and a *surfacted organic-based ferrofluids*, if the nanoparticle surface is sterically or electrosterically stabilized [3].

The surfactants used for steric stabilization have to be compatible with the carrier liquid and must overcome the attractive van der Waals and magnetic forces, which are usually present between the magnetic nanoparticles. Due to the magnetic dipolar attractions, unmodified magnetic nanoparticles tend to aggregate and inhibit the advantage of the specific single-domain properties. To prevent magnetic nanoparticles from aggregating, steric stabilization of their surface has to be performed [4].

A variety of monocarboxylic acids have been most often used for the steric stabilization of magnetic nanoparticles in an organic liquid medium. Monocarboxylic acids consist of a polar head, with an affinity for the hydrophilic particle surface, and a non-polar tail, with an affinity for the non-polar liquid medium.

Carboxylic functional groups can be adsorbed onto the surface of maghemite nanoparticles in different modes of coordination. In this regard, spectroscopic techniques such as infrared spectroscopy (IR) are most

often used to obtain information about the nature of the surface species and their mode of coordination.

The main goal of this work was to develop, characterize and optimize the process for the surface functionalization of superparamagnetic maghemite (γ-Fe$_2$O$_3$) nanoparticles with an organic coating and to determine the optimum amount of oleic acid for the most effective steric stabilization of nanoparticles.

With this aim, the mechanism of adsorption for surfactant molecules onto the nanoparticle surface in solution was carefully controlled using *in-situ* infrared spectroscopy (*React*IR), which provides a real-time, dynamic picture of the chemistry under actual reaction conditions and includes the possibility of analyzing the changes in the solution during the chemical reaction.

2 EXPERIMENTAL

Only commercially available reagents were used in this investigation. Iron (II) sulfate heptahydrate (FeSO$_4$ × 7H$_2$O, ACS, 99 + %; AlfaAesar), iron (III) sulfate hydrate (Fe$_2$(SO$_4$)$_3$ × xH$_2$O, Reagent Grade; AlfaAesar) and ammonium hydroxide solution (25 %, puriss p. a.; Fluka) were used as the starting reagents for the preparation of the nanoparticles. Oleic acid (cis-9-Octadecenoic acid, tech. 90 %, AlfaAesar) was used to provide the steric stabilization of the nanoparticles. n-Decane (CH$_3$(CH$_2$)$_8$CH$_3$; 99 + %; Alfa Aesar) served as the organic carrier liquid.

Maghemite (γ-Fe$_2$O$_3$) nanoparticles with an average particle size of around 12 nm were prepared using a classic coprecipitation method. Aqueous solutions of iron ions with a molar ratio x(Fe(II))/xFe(III)) = 1.5 were prepared by dissolving of an appropriate amount of iron (II) sulfate heptahydrate, FeSO$_4$ × 7H$_2$O, and iron (III) sulfate hydrate, Fe$_2$(SO$_4$)$_3$ × xH$_2$O in acidic conditions.

The synthesis occurred in a two-step process. In the first step, iron hydroxides were precipitated in an alkaline medium during the reaction between the aqueous solution of metal salts and an aqueous solution of ammonium hydroxide. In the final step of the synthesis the samples were oxidized and maghemite nanoparticles with a spinel structure were obtained. The temperature and the time of the reaction were kept constant at 25 °C and 1 h, respectively.

The synthesized maghemite nanoparticles were characterized using transmission electron microscopy (TEM, Jeol 2000–FX), X-ray diffractometry (XRD,
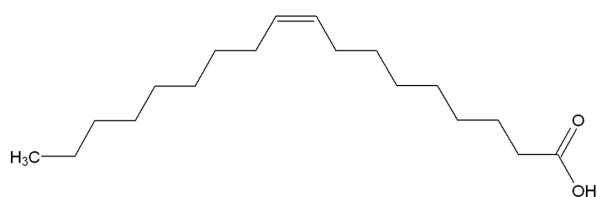
Brucker D4 Endeavour) and specific surface area measurements (BET, Micromeritis, Tristar 3000). The specific magnetization (Magneto – Susceptometer, DSM10) as a function of applied magnetic field at room temperature was also measured for all the prepared samples.

The functionalization process of the maghemite nanoparticle surface with oleic acid (OA) was performed in a solution of maghemite nanoparticles at room temperature within 30 minute intervals using *in-situ* infrared spectroscopy (**Figure 1**). The concentration of the surfactant was varied from the mass fraction 1.5 % to 4.0 % per mass unit of maghemite nanoparticles.

The mechanism of the adsorption of carboxylic acid onto the nanoparticle surface was investigated in solution using *in-situ* infrared spectroscopy.

The coated maghemite nanoparticles were finally dispersed into a small amount of carrier liquid ($\approx$18 % of n-decane per mass unit of maghemite nanoparticles) to obtain a stable and magnetically strong ferrofluid. n-Decane was used as the carrier liquid because of its low viscosity, low vapor pressure and chemical inertness.

The prepared ferrofluid samples were characterized using transmission electron microscopy and magnetometry.

3 RESULTS AND DISCUSSION

Figure 2 shows the characteristic XRD pattern of the maghemite nanoparticles obtained during the synthesis. The prepared maghemite samples showed very broad diffraction lines, in accordance with their small particle size and high specific surface area.
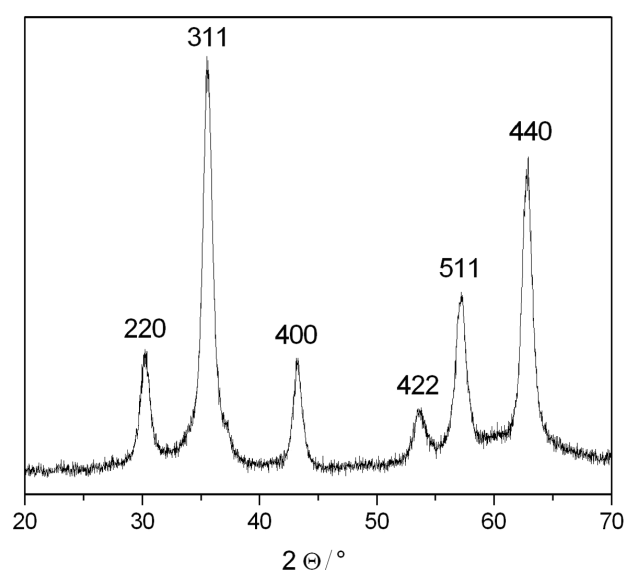

Figure 1: Chemical structure of oleic acid
Slika 1: Kemijska struktura oleinske kisline

Figure 2: X-ray diffraction pattern of maghemite (γ-Fe$_2$O$_3$) nanoparticles
Slika 2: Rentgenski difraktogram nanodelcev maghemita (γ-Fe$_2$O$_3$)

The average particle size determined from the specific surface area measurements (BET), was a little higher than the average particle size established from the (311) diffraction line broadening (**Table 1**), indicating that the particles were slightly agglomerated (**Figure 3**).

Table 1: Specific surface area (BET) and average particle size obtained from BET (D_{BET}) and XRD (D_{XRD})
Tabela 1: Specifična površina (BET) in povprečna velikost delcev določena z BET (D_{BET}) in XRD (D_{XRD})

Sample	BET/(m^2/g)	D_{BET}/nm	D_{XRD}/nm
γ-Fe$_2$O$_3$	68 ± 0.2	17 ± 0.1	12 ± 2

Figure 3 shows TEM images of uncoated partially agglomerated maghemite nanoparticles (a), and of maghemite nanoparticles obtained after the functionalization process (b), with a thin organic layer preventing the particles from agglomerating.

Figure 4 shows the IR spectra of pure oleic acid (OA) and maghemite (γ-Fe$_2$O$_3$) nanoparticles coated with OA. The spectrum of γ-Fe$_2$O$_3$ nanoparticles coated with OA was imitated after the functionalization process, 1 h after the addition of the mass fraction 3.4 % of OA per mass unit of γ-Fe$_2$O$_3$ nanoparticles in the solution of the synthesized nanoparticles.

It is worth noting that the C=O stretch presented at 1713 cm^{-1} in the spectra of pure OA was absent in the spectra of the coated nanoparticles and acid adsorbed onto their surface. Furthermore, there were two bands at 1646 cm^{-1} and 1351 cm^{-1}, characteristic for the symmetric ν_s(COO$^-$) and the asymmetric ν_{as}(COO$^-$) stretch, respectively [5].

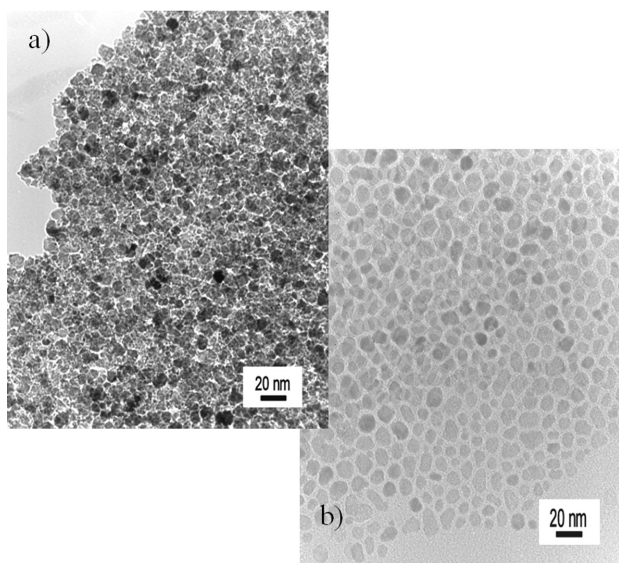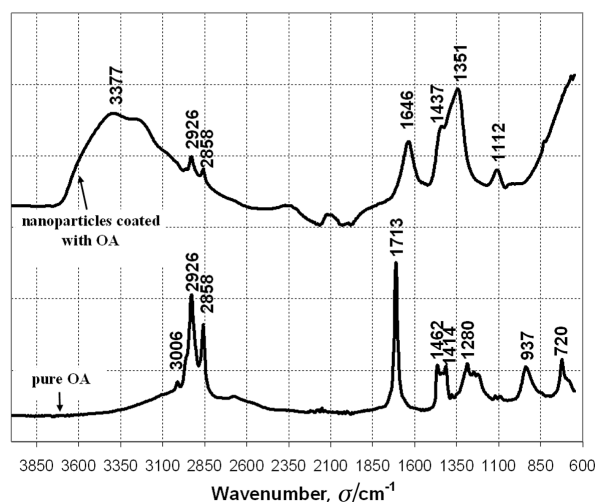This finding indicates that carboxylic acid is chemisorbed onto the nanoparticle surface in carboxylate form

Figure 4: IR spectra of pure OA and maghemite (γ-Fe$_2$O$_3$) nanoparticles coated with OA
Slika 4: IR-spektri čiste OA ter nanodelcev maghemita (γ-Fe$_2$O$_3$), oblečenih z OA
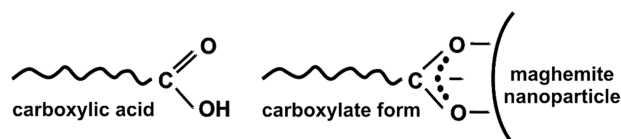

Figure 5: Chemisorption of carboxylic acid onto the maghemite nanoparticle surface
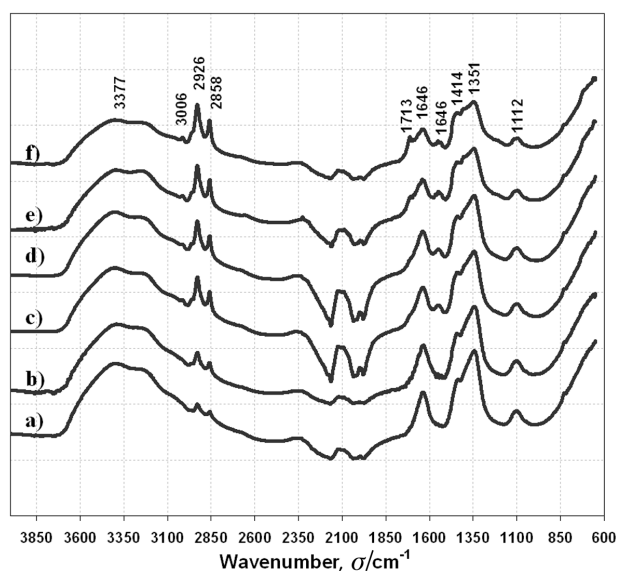**Slika 5:** Kemisorpcija karboksilne kisline na površino maghemitnih nanodelcev

Figure 3: TEM images of a) uncoated and b) coated maghemite (γ-Fe$_2$O$_3$) nanoparticles
Slika 3: TEM-posnetek a) neoblečenih in b) oblečenih nanodelcev maghemita (γ-Fe$_2$O$_3$)

Figure 6: IR spectra of γ-Fe$_2$O$_3$ nanoparticles coated with different amounts of OA in mass fractions: a) 1.5 %, b) 2 %, c) 2.9 %, d) 3.4 %, e) 3.7 %, f) 4 % OA per mass unit of maghemite nanoparticles
Slika 6: IR-spektri maghemitnih γ-Fe$_2$O$_3$ nanodelcev po oblačenju z različnimi masnimi deleži OA: a) 1,5 %, b) 2 %, c) 2,9 %, d) 3,4 %, e) 3,7 %, f) 4 %
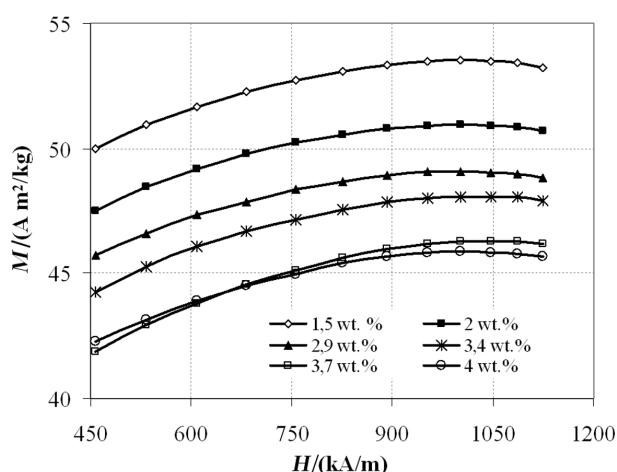
Figure 7: The specific magnetization of the prepared maghemite nanoparticles coated with different amounts of oleic acid
Slika 7: Specifična magnetizacija maghemitnih nanodelcev oblečenih z različnimi masnimi deleži oleinske kisline

(**Figure 5**), with two oxygen atoms that are symmetrically coordinated to the nanoparticle surface [6,7,8].

These results reveal the significance of surface interactions between the surfactant molecules and the nanoparticle surface for the preparation of organic-based ferrofluids. Furthermore, the appropriate amount of OA required for the most effective steric stabilization of the nanoparticles was also investigated.

Figure 6 presents the infrared spectra of γ-Fe$_2$O$_3$ nanoparticles coated with different amounts of OA, imitated after the functionalization process in the solution. The most characteristic peak of pure OA at 1713 cm^{-1} in Figure 4 was absent in **Figure 6** for a content of OA below the mass fraction 3.4 % per mass unit of γ-Fe$_2$O$_3$ nanoparticles, indicating that all the OA molecules were chemisorbed onto the nanoparticle surface.

With further increases of the OA content above 3.7 % per mass unit of γ-Fe$_2$O$_3$ nanoparticles, the characteristic peak of pure OA appeared, indicating that free molecules of OA were present in the solution.

From this we can conclude that a content of 3.7 % of OA per mass unit of γ-Fe$_2$O$_3$ nanoparticles represents the maximum content of OA to obtain the most effective steric stabilization of γ-Fe$_2$O$_3$ nanoparticles in order to prepare an organic-based ferrofluid with a high specific magnetization.

The specific magnetization of the prepared γ-Fe$_2$O$_3$ nanoparticles was around 59 A m^2/kg. **Figure 7** shows the specific magnetization of the prepared γ-Fe$_2$O$_3$ nanoparticles coated with different amounts of OA. With an increasing content of OA, the specific magnetization of the coated γ-Fe$_2$O$_3$ nanoparticles decreased from 53 A m^2/kg for the samples prepared with 1.5 % of OA per mass unit of γ-Fe$_2$O$_3$ nanoparticles to 46 A m^2/kg for the samples prepared with 4 % of OA per mass unit of

γ-Fe$_2$O$_3$ nanoparticles due to the increasing thickness of the nonmagnetic carboxylate shell. With an increasing content of OA above 3.7 % of OA per mass unit of γ-Fe$_2$O$_3$ nanoparticles, the nanoparticles were completely coated and the specific magnetization was stabilized at 46 A m^2/kg.

The specific magnetization of the ferrofluid sample, prepared from γ-Fe$_2$O$_3$ nanoparticles coated with 3.7 % of OA per mass unit of γ-Fe$_2$O$_3$ nanoparticles and dispersed in n-Decane as a carrier liquid, was around 38 A m^2/kg.

4 CONCLUSIONS

The adsorption of oleic acid (OA) onto the surface of maghemite (γ-Fe$_2$O$_3$) nanoparticles, which is of great importance for the preparation of ferrofluids, was investigated in solution using *in-situ* infrared spectroscopy. The results indicated that hydrophilic head–groups of oleic acid were chemisorbed onto the nanoparticle surface in a carboxylate form with two oxygen atoms that are symmetrically coordinated to the nanoparticle surface.

The most effective steric stabilization of γ-Fe$_2$O$_3$ nanoparticles was obtained in the range between mass fractions 1.5 % and 3.4 % of OA per mass unit of γ-Fe$_2$O$_3$ nanoparticles. In-situ IR spectroscopy was shown as an applicable method for determining the appropriate amount of surfactant molecules required for the steric stabilization of maghemite nanoparticles in a carrier liquid.

The specific magnetization of the prepared g-Fe$_2$O$_3$ nanoparticles was around 59 A m^2/kg and decreased to 46 A m^2/kg for the γ-Fe$_2$O$_3$ nanoparticles coated with 4 % of OA per mass unit of γ-Fe$_2$O$_3$ nanoparticles due to the nonmagnetic carboxylate shell. The specific magnetization of the ferrofluid sample, prepared from γ-Fe$_2$O$_3$ nanoparticles coated with 3.7 % of OA per mass unit of γ-Fe$_2$O$_3$ nanoparticles and dispersed in n-Decane as a carrier liquid, was around 38 A m^2/kg.

5 REFERENCES

[1] D. Makovec, A. Košak, A. Žnidaršič, M. Drofenik, The synthesis of spinel-ferrite nanoparticles using precipitation in microemulsions for ferrofluid applications, J. Magn. Magn. Mater., 289 (**2005**), 32–35

[2] S. Monet, F. Grasset, J. Portier and E. Duguet: Maghemite@silica nanoparticles for biological applications, European Cells and Materials, 3 (**2002**)2, 110–113

[3] C. Scherer and A. M. Figueiredo Neto, Ferrofluids: Properties and applications, Brazilian Journal of Physics, 35 (**2005**) 3A

[4] Yongkang Sun, Lei Duan, Zhirui Guo, Yun Duan Mu, Ming Ma, Lina Xu, Yu Zhang, Ning Gu: An improved way to prepare superparamagnetic magnetite-silica core-shell nanoparticles for possible biological application, Journal of Magnetism and Magnetic Materials 285 (**2005**), 65–70

[5] Nianqiang Wu, Lei Fu, Ming Su, Mohammed Aslam, Ka Chun Wong, and Vinayak P. Dravid: Interaction of fatty acid monolayers with cobalt nanoparticles, Nano Letters, 4 (**2004**) 2, 383–386

[6] Tapan K. Jain, Marco A. Morales, Sanjeeb K. Sahoo, Diandra L. Leslie-Pelecky, Vinod Labhasetwar, Iron oxide nanoparticles for sustained delivery of anticancer agents, Molecular Pharmaceutics, 2 (**2005**)3, 194–205

[7] Ling Zhang, Rong He, Hong-Chen Gu: Oleic acid coating on the monodisperse magnetite nanoparticles, Applied Surface Science 253 (**2006**), 2611–2617

[8] Shi Yu and Gan Moog Chow: Carboxyl group (-CO$_2$H) functionalized ferrimagnetic iron oxide nanoparticles for potential bio-applications, Journal of Materials Chemistry, 14 (**2004**), 2781–2786

ANALYSIS OF THE TEMPERATURE PROFILES DURING THE COMBUSTION SYNTHESIS OF DOPED LANTHANUM GALLATE

ANALIZA TEMPERATURNIH PROFILOV MED ZGOREVALNO SINTEZO DOPIRANEGA LANTANOVEGA GALATA

Marjan Marinšek

Faculty of Chemistry and Chemical Technology, Aškerčeva 5, 1000 Ljubljana, Slovenia
marjan.marinsek@fkkt.uni-lj.si

Strontium-, magnesium-, iron-doped lanthanum gallate was prepared by the citrate-nitrate combustion technique. The temperature profiles of the citrate-nitrate metal ions system were measured and analyzed by applying the Boddington method. On the basis of the temperature measurements it was possible to perform thermodynamic and kinetic analysis of the system. The Boddington parameters T_c, u, t_r, t_d, t_x, t^*, τ_{ad}, α, G that are essential for the kinetic analysis were defined by means of calculated λ, h, c_p values of the combustion system and measured values of ρ and Q. Arrhenius kinetics was assumed for the determination of the kinetic parameters such as the activation energy E_a, the expotential factor n and pre-expotential factor K_0' of the system. The activation energy for the combustion system was determined by the method of combustion-wave propagation velocity to be 34.8 kJ mol^{-1}, by the Boddington method to be 31.8 kJ mol^{-1} and by the Freeman-Carroll method to be 33.1 kJ mol^{-1}.

Key words: lanthanum gallate, self-propagating-high-temperature synthesis, citrate-nitrate combustion process, kinetic analysis, the Boddington method, Freeman-Carrol

Lantanov galat, dopiran s stroncijem, magnezijem in železom, je bil pripravljen po citratno-nitratnem postopku zgorevalne sinteze. Merjeni temperaturni profili sistema citrat-nitrat-kovinski ioni so bili analizirani po Boddingtonovi metodi. Na podlagi izračunanih vrednosti λ, h, c_p zgorevalnega sistema in merjenih vrednosti ρ in Q so bili določeni Boddingtonovi parametri T_c, u, t_r, t_d, t_x, t^*, τ_{ad}, α, G, ki so kjučnega pomena za kinetično analizo. Za določitev kinetičnih parametrov, kot so aktivacijska energija E_a, eksponentni faktor n in predeksponentni faktor K_0' sistema, je bila predpostavljena Arrheniusova kinetika. Aktivacijska energija je bila določena po metodi hitrosti napredovanja zgorevalnega vala v odvisnosti od temperature z vrednostjo 34,8 kJ mol^{-1}, po Boddingtonovi metodi z vrednostjo 31,8 kJ mol^{-1} in po Freeman-Carrollovi metodi z rezultatom 33,1 kJ mol^{-1}.

Ključne beside: lantanov galat, zgorevalna sinteza, citratno-nitratni postopek, kinetična analiza, Boddingtonova metoda, metoda Freeman-Carrol

1 INTRODUCTION

Lately, the oxygen ionic transfer in some doped perovskite-type oxides was investigated with special emphasis on the relationship between the oxygen-ion conductivity and the material lattice parameters [1-3]. Among the investigated materials gallate ABO_3 with A = La was found to have the highest Goldschmidt tolerance factor and correspondingly the highest oxygen ionic conductivity in relation to other A = rare-earth occupations. On the B-site, the maximum specific conductivity and oxygen transfer and the minimum of the activation energy were determined in the case of Ga [4,5]. The ionic conductivity properties of perovskites were explained in terms of their structure, i.e., the oxygen ionic conductivity increases with the free volume of the unit cell and decreases with decreasing tolerance factor owing to an increasing distortion of the perovskite structure.

The oxygen ionic conductivity of lanthanum gallates can be improved with appropriate doping owing to the generation of oxygen vacancies. Among the dopands Sr (A-site dopand) and Mg (B-site dopand) additions ($La_{0.9}Sr_{0.1}Ga_{0.8}Mg_{0.2}O_{3-x}$) were found to have a profound effect on increasing the oxygen ionic conductivity – LSGM [6]. If Ga in $La_{0.9}Sr_{0.1}(Ga_{1-y}M_y)_{0.8}Mg_{0.2}O_{3-x}$ is further substituted by a transition metal (M = Cr, Mn, Fe, Co), the electrical properties of LSGM can be further modified. When doped with amounts $y \leq 0.1$ of Fe or Co, gallates exhibit oxygen ionic conductivities twice that of LSGM [7], which enables these materials to be used as medium-temperature electrolytes. With increasing dopant concentration both the exchangeable oxygen and the p-type electrical conductivity increase, which is of interest for applications as mixed conductors.

Doped lanthanum gallates are usually prepared either from the corresponding oxides with a solid-state reaction at high temperatures [8,9], or with self-propagating high-temperature synthesis (SHS) [10]. Such solid-state reactions are diffusion controlled and time consuming, while the resulting powders may show a certain degree of compositional inhomogeneity. In contrast, a combustion synthesis or a self-propagating high-temperature synthesis (SHS) provides an attractive practical alternative to conventional methods. The combustion process involves the decomposition of a redox system, which then proceeds as a self-sustaining front throughout the

reactant gel mixture. The reaction conditions and the large amount of heat evolved during the reaction enable the direct production of a large number of single or multicomponent crystalline and homogeneous powders that have a narrow particle size distribution [11]. From the variety of possible redox systems, a combustion mixture based on the citrate-nitrate combination can be potentially applied for the production of larger quantities of mixed oxides owing to its relatively non-violent combustion [12].

The theoretical physical models that explain, simulate and predict SHS reaction phenomena are based on energy and mass balances [13]. In the case where the reaction rate is used to calculate the kinetic parameters of the reaction, several mathematical models have been developed. In this respect the Boddington method [14] is particularly valuable because calculations of the kinetic parameters and the preliminary thermal conductivity determinations are not necessary. Moreover, the Boddington method is not based on a specific kinetic model but predicts the same kinetic behaviour of the system at a certain value of the reactant-to-product conversion. The origin of the Boddington method is thus a mathematical analysis of the measured temperature profiles of the combustion system with respect to the heat-balance equation utilized. The Boddington method employs the following heat-balance equation:

$$\kappa \frac{\partial^2 T}{\partial x^2} - C_p \rho \frac{\partial T}{\partial t} + \Phi(T, \eta) - h(T - T_0) = 0 \qquad (1)$$

In the above equation C_p is the heat capacity of the product, ρ is its density, κ is the thermal conductivity, $\Phi'(T,\eta)$ is the rate of heat generation, h is an axial heat-transfer coefficient, T is the temperature, t is the time and x is the coordinate of wave propagation (the radiant heat losses are assumed to be negligible). The result of a combustion temperature profile according to the Boddington method is the calculation of the previously mentioned parameters, which finally enables a determination of the activation energy for the combustion reaction.

When the data on the fraction reacted η vs. T or t are accessible, several approaches are available for the kinetic analysis. A particularly interesting approach to kinetic parameter determination, because of its simplicity, is the Freeman-Carroll method [15]. This method is based on Arrhenius kinetics and utilizes the following kinetic function:

$$\frac{d\eta}{dt} = K_0' \exp\left(-\frac{E}{RT}\right)(1-\eta)^n \qquad (2)$$

where K_0' is a constant and n is an exponential factor in a function of the kinetic order.

In the present work, a citrate-nitrate (fuel-oxidant) combustion synthesis method was employed to produce $La_{0.85}Sr_{0.1}(Ga_{0.9}Fe_{0.1})_{0.8}Mg_{0.2}O_{3-\delta}$ (LSGFM) To our knowledge, this is the first time that combustion synthesis was

chosen for doped-LSGM preparation. The citrate-nitrate system was chosen due to its non-violent nature and because fine-doped LSGM-based perovskites have potential uses in the previously mentioned applications. For the chosen combustion system a complete Boddington analysis was also performed.

2 EXPERIMENTAL PROCEDURE

$La_{0.85}Sr_{0.1}(Ga_{0.9}Fe_{0.1})_{0.8}Mg_{0.2}O_{3-x+\delta}$ perovskite was prepared with a modified combustion synthesis based on the citrate-nitrate redox reaction. The starting substances for the reactive gel preparation were $La(NO_3)_3 \cdot 6H_2O$, $Sr(NO_3)_2$, $Ga(NO_3)_3 \cdot 10H_2O$, $Mg(NO_3)_2 \cdot 6H_2O$, $Fe(NO_3)_3 \cdot 9H_2O$, $C_6H_8O_7 \cdot H_2O$, and nitric acid (analytical reagent grade). $La(NO_3)_3 \cdot 6H_2O$ (3.000 g), $Sr(NO_3)_2$ (0.173 g), $Ga(NO_3)_3 \cdot 10H_2O$ (2.559 g), $Mg(NO_3)_2 \cdot 6H_2O$ (0.417 g), $Fe(NO_3)_3 \cdot 9H_2O$ (0.263) and $C_6H_8O_7 \cdot H_2O$ (2.394 g) were dissolved separately with minimum additions of water in amounts that ensured the desired final composition. Aqueous solutions were mixed and HNO_3 (aq. 65 %, 1.25 mL)) was added to ensure the initial citrate/nitrate molar ratio of 0.18. With the aim to obtain kinetic parameters from the temperature profile measurements, the reaction system was then diluted with different additions of α-Al_2O_3 (from 0 % Al_2O_3 up to 5 % Al_2O_3 in the dry reactive mixture). A suspension (mixed nitrate solution with Al_2O_3 addition) was kept over a water bath at 60 °C under vacuum (5 mbar) until it transformed into a bright fragile xerogel.

The dried and diluted gels were gently milled and homogenized in an agate mortar and subsequently uniaxially pressed (17 MPa) into pellets (16 mm in diameter, height $\approx$30 mm). The pellets were ignited at the top to start a self-sustaining combustion reaction producing doped LSGM perovskite. If the additions of Al_2O_3 exceeded 5 % the combustion system did not react in a self-sustaining mode.

The temperature profiles of the burning tablets were measured using an optical pyrometer (Ircon, model IPE 140, based on sample brightness) with a measuring range from 50 to 1200 °C and a very quick response time (1.5 ms). The accuracy of the optically measured temperature was ±2.5 °C below 400 °C and ±0.4 % of the measured value (in °C) above 400 °C. Since the measured systems were all ceramics with unknown exact emissivities, the emissivity was set to 0.85 and was kept constant for all the measurements. This value is close to the cited emissivities of ceramic products and Al_2O_3 in the measured temperature range. The temperature profiles of the reaction systems were measured from a distance of 10 cm with a space resolution of temperature measurements (the size of the measured spot on the sample surface) of 0.3 mm. Prior to the Boddington kinetic analysis, the experimentally measured temperature profiles were smoothed in the zone of rapid temperature change. The smoothing procedure is essential because
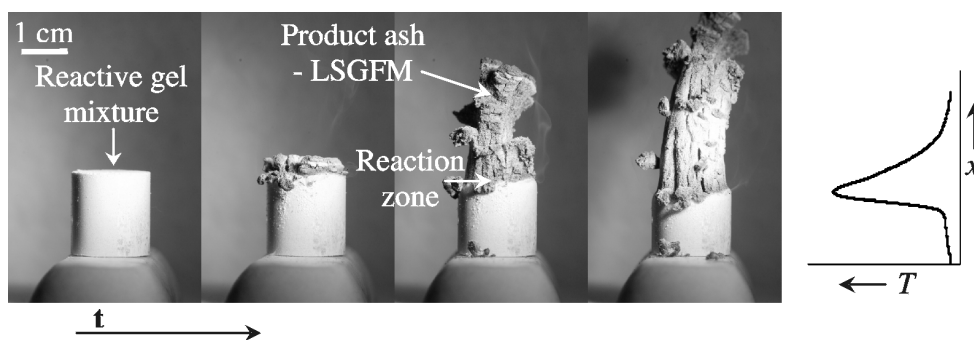
Figure 1: Self-sustaining citrate-nitrate reaction for $La_{0.85}Sr_{0.1}(Ga_{0.9}Fe_{0.1})_{0.8}Mg_{0.2}O_{3-x+\delta}$ preparation
Slika 1: Napredovanje zgorevlne sinteze v sistemu za pripravo $La_{0.85}Sr_{0.1}(Ga_{0.9}Fe_{0.1})_{0.8}Mg_{0.2}O_{3-x+\delta}$

the measured values may oscillate around an average value, which makes the analysis of the temperature profile difficult. Slight temperature oscillations were ascribed to the surface roughness and to the synthesized material porosity.

3 RESULTS AND DISCUSSION

Combustion synthesis is a relatively new approach to doped-gallate preparation, i.e., gallates are normally prepared via a solid-state reaction. Very few reports are found in the literature describing lanthanum-gallate-based materials prepared via a combustion route [16,17] and none deal with citrate-nitrate-derived doped lanthanum gallates.

One of the reasons why citrate-nitrate combustion synthesis for doped gallates preparation was neglected is that the preparation of pure lanthanum gallate is practically impossible. Regardless of the citrate/nitrate (c/n) molar ratio used (from fuel-lean $0.13 < c/n < 0.25$ to fuel-rich mixtures $0.25 < c/n < 0.33$) or small additions of various fuels (e.g. urea), the heat evolved during the combustion was not sufficient to trigger a self-sustaining combustion reaction. Only if dopand elements (Fe or Co) that are known for their catalytic activity towards citrate-nitrate combustion are added to the fuel-lean initial mixture (c/n = 0.18) can the self-sustaining combustion be achieved (**Figure 1**). Such a system was then the basis for the Boddington kinetic analysis.

To confirm citrate-nitrate combustion as an appropriate synthesis route for LSGFM preparation, the final ash product, as well as the intermediate products, was submitted for XRD analysis (**Figure 2**). Intermediates were prepared by careful heating of small amounts of the initial xerogel in air up to a predetermined temperature. According to **Figure 2** it is apparent that the intermediate precursors were amorphous at temperatures below 740 °C. At higher temperatures some crystalline phases appeared. The main crystalline phase found in intermediates treated above 740 °C was identified as the perovskite $La_{0.895}Sr_{0.105}Ga_{0.8}Mg_{0.2}O_{3-\delta}$. Additionally, only traces of residual secondary phases

$SrLaGa_3O_7$ and $SrLaGaO_4$ were found with XRD. If the intermediate preparation temperatures ware increased, the secondary phases were almost completely dissolved in the LSGFM perovskite structure. The relatively low amounts of secondary phases in the intermediates prepared above 740 °C make, in our opinion, the combustion synthesis favourable when compared to preparation processes that are based on the diffusion of components in the solid state (in the latter case the amount of secondary phases is normally greater).

The entire range of as-measured temperature profiles for the chosen citrate-nitrate combustion system with different additions of Al_2O_3 diluting agent (λ) are shown in **Figure 3**. Altering the amount of diluting agent influences many parameters pertaining to the combustion reaction, such as the wave velocity and the combustion temperature, as summarized in **Table 1**. According to the results in **Figure 3 and Table 1**, a greater addition of diluting agent lowers the peak combustion temperature, as well as the rate of propagation of the combustion reaction. However, the general shape of the temperature profile did not change with any variation in the amount of diluent. Another interesting fact is the relatively rapid
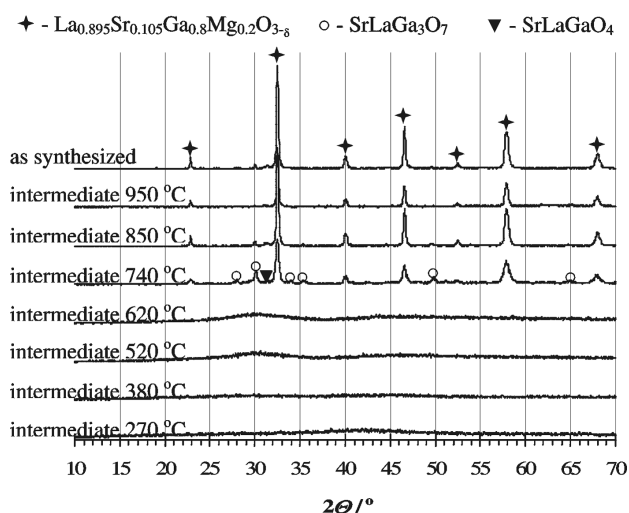

Figure 2: XRD patterns of intermediates and as-synthesized LSGFM
Slika 2: Rentgenogrami vmesnih produktov ter LSGFM sintetizira-nega materiala

product cooling. The samples cooled down from their peak temperature to 50 °C in approximately 40–60 s. The fast cooling was ascribed to the very porous structure formed after the combustion (**Figure 1**). The determination of the parameters' peak combustion temperature (T_c) and the combustion propagation velocity (u) is essential for the wave-velocity analysis. For the activation-energy calculation the following equation was utilized:

$$\frac{u^2}{T_c^2}(1-\lambda) = f(\eta)K_0\alpha\frac{C_p}{Q_0}\frac{R}{E}\exp\left(-\frac{E}{RT_c}\right)$$

where $f(\eta)$ is a function that depends on the kinetic order of the reaction, α is the thermal diffusivity of the product, C_p is the heat capacity of the product, Q_0 is the heat of reaction for an undiluted system, λ is the weight fraction of diluent, E is the activation energy, R is the general gas constant and K_0 is a constant. As the parameters u and T_c are altered if the reaction system is diluted with an inert substance, the activation energy can then be calculated from the slope in the plot of ln $((1-\lambda)^{0.5}(u/T_c))$ vs. $1/T_c$. From the best-fit linear slope of the experimental combustion parameters, an apparent combustion activation energy of 34.8 kJ/mol was calculated (**Figure 4**).

Table 1: Reaction parameters of citrate-nitrate SHS systems
Tabela 1: Parametri citratno-nitratne zgorevalne reakcije

λ/wt	T_c/K	$u \cdot 10^3$ /(cm s^{-1})	$(\partial T/\partial t)$ /K·s^{-1}	$(\partial T/\partial$xt) /K·cm^{-1}
0	907.2	18.33	177	9655
0.01	871.5	19.71	149	7557
0.02	834.6	17.07	146	8552
0.03	725.5	12.17	129	10596
0.04	715.7	9.09	103	11329
0.05	700.5	7.63	96	12575

In order to obtain kinetic information from the temperature profiles, a variety of calculations were performed on the basis of the experimental data. First, the temperature profiles in the zone of rapid temperature change were smoothed. From the smoothed version of the temperature profiles, the first and the second derivatives $\partial T/\partial t$ and $\partial^2 T/\partial t^2$ of each smoothed profile were calculated. The peak value in the plot of $\partial T/\partial t$ vs. t corresponds to the maximum heating rate achieved during the reaction. If this value were divided by the measured wave-velocity value (u), the maximum thermal gradient $(\partial T/\partial x)_{max}$ in the propagating coordinate could be calculated (**Table 1**).

Then a complete Boddington analysis [14] of the temperature profiles obtained was performed, including the calculations of t_r and t_d (the rise time of a general adiabatic fore-wave and the remote decay time, respectively) in order to determine the two other values t_x (thermal relaxation time) and t^* using the relationships $t_x = t_d - t_r$ and $1/t^* = 1/t_r - 1/t_d$. The parameters t_x and t^* include the thermodynamic values and can be further expressed as $t^* = \alpha/u^2$ and $t_x = \rho C_p/h$, where α represents the effective thermal diffusivity (**Table 2**).

Table 2: Experimentally determined parameters of the Boddington analysis for the citrate-nitrate combustion
Tabela 2: Parametri citratno-nitratne zgorevalne reakcije določeni z Boddingtonovo metodo

λ/wt	t_d/s	t_d/s	t_x/s	t^*/s	τ_{ad}/K	$\alpha \cdot 10^3$ /cm^2·s^{-1}
0	2.579	11.274	8.695	3.343	1392	1.124
0.01	2.369	12.005	9.636	2.951	1319	1.147
0.02	2.968	13.351	10.383	3.817	1296	1.113
0.03	2.952	13.850	10.898	3.752	1271	0.556
0.04	4.625	14.327	9.701	6.831	1222	0.565
0.05	5.733	15.432	9.698	9.124	1093	0.532

The temperature rise of the combustion system without heat losses, the value τ_{ad} (**Table 2**), was calculated by integrating the temperature profile, as described in [18]. If the combustion system is under adiabatic
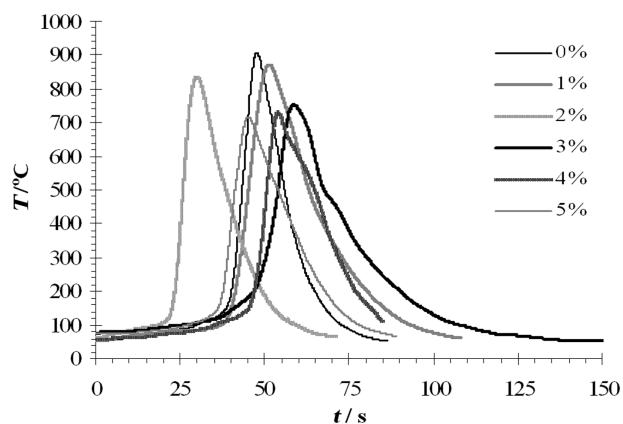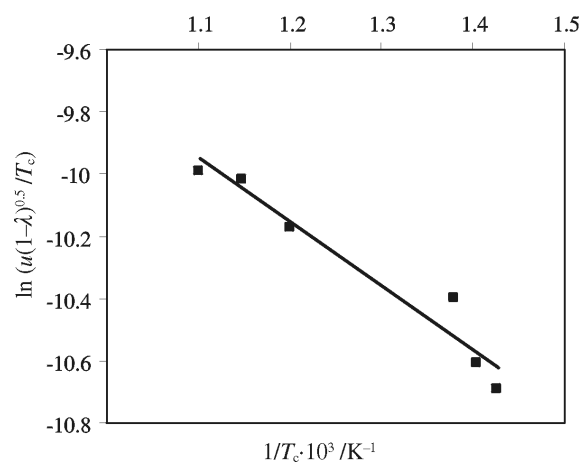

Figure 3: Measured temperature profiles of citrate-nitrate SHS systems with different additions of diluent
Slika 3: Merjeni temperaturni profili citratno-nitratnega sistema z različnimi dodatki sredstva za redčenje

Figure 4: Wave-velocity analysis for combustion-derived LSGFM with different additions of Al$_2$O$_3$
Slika 4: Analiza hitrosti napredovanja zgorevalnega vala za sintezo LSGFM ob različnih dodatkih Al$_2$O$_3$

conditions, the value of $\tau_{ad.}$ should be close to the value of T_c. However, if data from **Tables 1 and 2** are compared, $\tau_{ad.}$ and T_c differ substantially. One reason for this is the incompletely adiabatic conditions during the reaction, i.e., during the citrate-nitrate combustion some volatile products are also formed [19], carrying off a certain amount of heat. This implies that Eq. (1) should be changed in such a way as to describe the heat balance of the citrate-nitrate combustion, also taking into account the heat losses due to hot-gas formation. Nevertheless, the proposed Boddington heat-balance equation can still be used for the kinetic analysis and for the estimation of the η vs. T (or t) relationship (**Figure 5**). The function η vs. t was calculated in accordance with the following re-arranged Boddington heat-balance equation:

$$G = t_x^{-1}(T - T_0) + \partial T/\partial t - t * \partial^2 T/\partial t^2$$

Since G also equals $t_{ad}(\partial\eta/\partial t)$, it was possible to calculate the reaction rate by dividing the values of G by the adiabatic temperature rise. Finally, by integrating the experimentally determined reaction rate, the fraction reacted η was calculated.

The calculated η vs. t data showed that the citrate-nitrate combustion is a relatively rapid process. In an undiluted sample the elapsed time interval from 10 % conversion to 90 % conversion was approximately 4.1 seconds, or, expressed in distance, equal to 0.75 mm.

The kinetic parameters obtained were used to calculate the activation energy of the citrate-nitrate combustion process. Due to the dependence of the T–η relationship on inert diluent additions [14], the activation energy could be calculated by plotting the experimentally determined values of $\partial\eta/\partial t$ vs. the reciprocal of the absolute temperature at a fixed value of η. The magnitude of the slope in such a diagram should equal -E/R. The temperature dependence of the reaction rate at
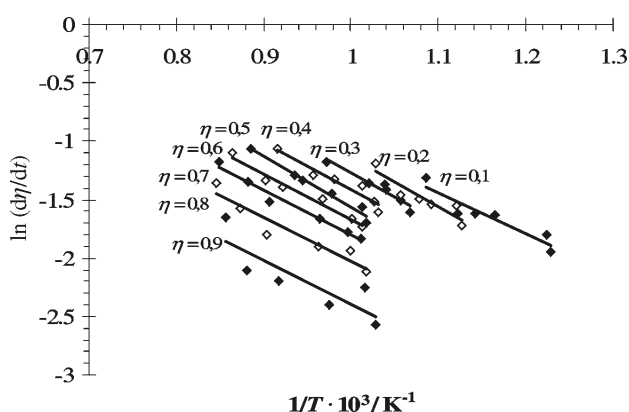
Figure 6: Temperature dependence of the reaction rate ln ($\partial T/\partial t$) for different values of η in the citrate-nitrate combustion system
Slika 6: Temperaturna odvisnost reakcijske hitrosti ln ($\partial T/\partial t$) pri različnih vrednostih η v citratno-nitratnem zgorevalnem sistemu

different η values is shown in **Figure 6**. From this it is evident that the slopes of the middle data sets (from $\eta = 0.4$ to $\eta = 0.8$) agree fairly well with each other. On the other hand, the slopes at lower values of η (from $\eta = 0.1$ to $\eta = 0.3$) and the slopes at the highest η values ($\eta = 0.9$) exhibited different (normally slightly lower) values compared to the middle data sets. Taking into account only the slopes of the middle data sets, the activation energy of 31.8 kJ/mol was deduced for the citrate-nitrate combustion system.

The third technique used for the kinetic analysis of the investigated citrate-nitrate system was the Freeman-Carroll method [15]. When predetermined $\partial\eta/\partial t$ vs. T data are used, this method enables the activation energy to be determined, as well as the parameters n and K_0' from Eq. (2). First, the parameter n was calculated from the slope in the plot of (Δ ln ($d\eta/dt$))/(Δ 1/T) vs. (Δ ln (1–η))/(Δ 1/T). Then the activation energy and the parameter K_0' of the system were calculated from the plots of ln ($d\eta/dt \cdot 1/(1-\eta)^n$) vs. the reciprocal of the absolute temperature. The magnitudes of the slope in such a diagram equal -E/R, while the intercept on the ordinate gives the value of ln K_0' (**Figure 7**). Parameters n, E and K_0' were determined for the undiluted system, as well as for all systems with various additions of diluent. The average n, K_0' and E values for all the investigated systems were calculated as (0.52, 5.97) s^{-1} and 33.1 kJ/mol, respectively.

The results of the calculation of the activation energy obtained from wave-velocity measurements (34.8 kJ/mol), the temperature-profile analysis (31.8 kJ/mol) and the Freeman-Carroll kinetic analysis (33.1 kJ/mol) are in good agreement, implying that any of the three techniques described can be used for a determination of the kinetic parameters. However, the good correlation between the E values obtained with different methods is not surprising, because all the methods are based on a similar assumption concerning the kinetic law (the Freeman-Carroll analysis uses data obtained from a
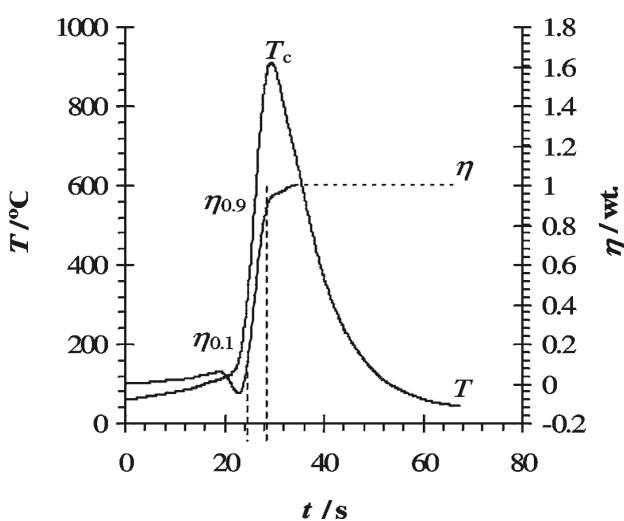

Figure 5: Temperature profile and time dependence of the fraction reacted for the undiluted sample
Slika 5: Merjeni temperaturni profil ter izračunana stopnja konverzije za pripravo LSGFM v neredčenem sistemu
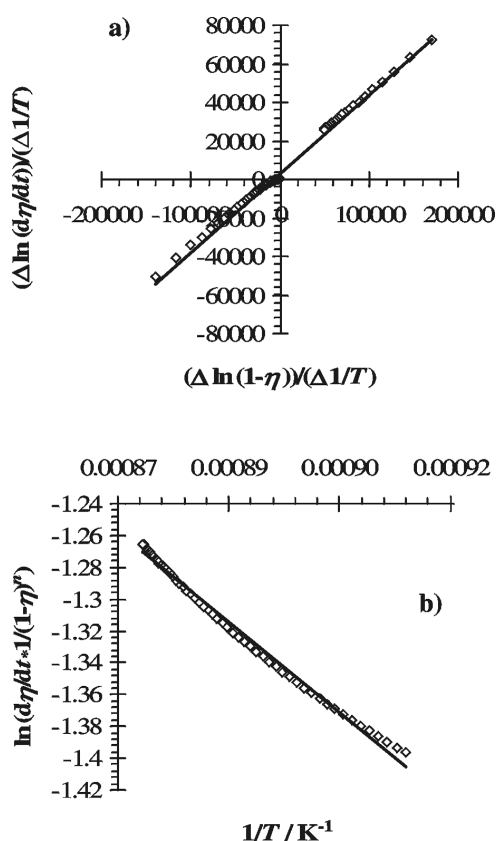
Figure 7: Determination of n, E and K_0' according to the Freeman-Carroll method, demonstration on a sample with $\lambda = 0.01$ wt.: a) determination of the parameter n, b) determination of K_0' and E

Slika 7: Določitev n, E in K_0' z metodo Freeman-Carroll v sistemu $\lambda = 0,01$ a) določitev parametra n, b) določitev K_0' in E

temperature-profile analysis). For a further validation the values of the kinetic parameters should be related to those deduced by applying an analogous or at least a similar method. As is implicit in the model on which the Boddington analysis is based, the processes which govern the rate of conversion are assumed to be chemical reactions and diffusion processes. Using this model all the reactions are treated simultaneously by applying a general function $f(\eta)$ that describes sufficiently the time dependence of the conversion equivalent h. The calculated value of the exponent n implies that there are several (at least two) processes that determine the rate of conversion. Either we have more than one reaction, each determined by its own kinetic law, affecting the rate, which leads to an overall exponent value of 0.5, or the diffusion process is the rate-limiting factor. This would also explain the relatively low value of the activation energy.

4 CONCLUSIONS

Sr-, Mg-, Fe-doped lanthanum gallate was prepared for the first time via citrate-nitrate combustion synthesis. This was successful only after the addition of an appropriate amount of a doping element, which is also catalytically active toward the citrate-nitrate combustion. The main benefits of combustion-derived powders are a single-step process that is relatively quick, and the practical absence of secondary phases in the LSGFM after the synthesis.

A kinetic analysis of the burning system was made using three methods – wave-velocity measurements, temperature-profile analysis and the Freeman-Carroll analysis – all based on the kinetic law. The kinetic parameters obtained with the different methods are in good agreement, meaning that any of the three techniques described can be used for determining the kinetic parameters. The average n and E calculated values (≈ 0.5 and 31–35 kJ/mol, respectively) may be denoted as apparent values, and this implies that the diffusion process is the probably the rate-limiting factor.

5 LITERATURE

[1] A. Manthiram, J. F. Kuo, J. B. Goodenough, *Characterization of oxygen-deficient perovskites as oxide-ion electrolytes*, Solid State Ionics, 62 (**1993**) 3–4, 225–234

[2] R. L. Cook, R.C. MacDuff, A. F. Sammells, *Perovskite solid electrolytes for intermediate temperature solid oxide fuel cells*, J. Electrochem. Soc., 137 (**1990**) 10, 3309–3310

[3] T. Ishihara, H. Matsuda, Y. Takita, *Doped LaGaO3 Perovskite type oxide as a new oxide ionic conductor*, J. Am. Chem. Soc., 116 (**1994**), 3801–3803

[4] T. Ishihara, H. Matsuda, M. Azmi bin Bustam, Y. Takita, Oxide-ion conductivity in doped Ga based perovskite-type oxide, Solid State Ionics, 86/88 (**1996**), 197–201

[5] K. Nomura, S. Tanase, Electrical conduction behavior in $(La_{0.9}Sr_{0.1})M^{III}O_{3-\#}$ (M^{III}=Al, Ga, Sc, In, and Lu) perovskites, Solid State Ionics, 98 (**1997**) 3, 229–236

[6] P. Huang, A. Petric, Superior oxygen ion conductivity of lanthanum gallate doped with strontium and magnesium, J. Electrochem. Soc., 143 (**1996**) 5, 1644–1648

[7] N. Trofimenko, H. Ullmann, *Transition metal doped lanthanum gallates*, Solid State Ionics, 118 (**1999**), 215–227

[8] N. Liu, Y. P. Yuan, P. Majewski, F. Aldinger, Sintering behaviour, mechanical properties and thermal shock resistance of alkaline earth doped lanthanum gallate, Powder Metallurgy, 49 (**2006**) 1, 34–39

[9] P. Datta, P. Majewski, F. Aldinger, Synthesis and characterization of strontium and magnesium substituted lanthanum gallate-nickel cermet anode for solid oxide fuel cells, Materials Chemistry and Physics, 102 (**2007**) 2–3, 125–131

[10] H. Ishikawa, M. Enoki, T. Ishihara, T. Akiyama, Self-propagating high-temperature synthesis of La(Sr)Ga(Mg)O3-δ for electrolyte of solid oxide fuel cells, Journal of Alloys and Compounds, 430 (**2007**) 1–2, 246–251

[11] L. A. Chick, L. R. Pederson, G. D. Maupin, J. L. Bates, L. E. Thomas, G. J. Exarhos, *Glycine-nitrate combustion synthesis of oxide ceramic powders*, Mater. Letters, 10 (**1990**) 1–2, 6–12

[12] S. R. Jain, K. C. Adiga, V. R. Pai Verneker, *A new approach to thermochemical calculations of condensed fuel-oxidizer mixtures*, Combustion and Flame, 40 (**1981**), 71–79

[13] J. J. Moore, H. J. Feng, Combustion synthesis of advanced materials: Part II. Classifications, applications and modeling, Progress in Material Science, 39 (**1995**), 275–316

[14] T. Boddington, P. G. Laye, J. Tipping, D. Whalley, *Kinetic analysis of temperature profiles for pyrotechnic systems*, Combust. Flame, 63 (**1986**), 359–368

[15] H. L. Freeman, B. J. Carroll, The Application of thermoanalytical techniques to reaction kinetics. The thermogravimetric evaluation of

the kinetics of the decomposition of calcium oxalate monohydrate, J. Phys. Chem., 62 (**1958**) 4, 394–397

[16] L. Cong, T. He, Y. Ji, P. Guan, Y. Huang, W. Su, Synthesis and characterization of IT-electrolyte with perovskite structure $La_{0.8}Sr_{0.2}Ga_{0.85}Mg_{0.15}O_{3-\delta}$ by glycine-nitrate combustion synthesis, Journal of Alloys and Compounds, 348 (**2003**), 325–331

[17] J. W. Stevenson, T. R. Armstrong, D. E. McCready, L. R. Pederson, W. J. Weber, Processing and electrical properties of alkaline earth-doped lanthanum gallate, J. Electrochem. Soc., 144 (**1997**) 10, 3613–3620

[18] S. D. Dunmead, Z. A. Munir, Temperature profile analysis in combustion synthesis: I, Theory and background, J. Am. Ceram. Soc., 75 (**1992**) 1, 175–179

[19] M. Marinšek, K. Zupan, J. Maček, Citrate-nitrate gel transformation behaviour during the synthesis of combustion derived NiO-YSZ composite, J. of Mater. Res., 18 (**2003**) 7, 1551–1560

A METALLOGRAPHIC EXAMINATION OF A FRACTURED CONNECTING ROD

METALOGRAFSKA PREISKAVA PRELOMA OJNICE

Roman Celin, Boris Arzenšek, Dimitrij Kmetič

Institute of Metals and Technology, Lepi pot 11, 1000 Ljubljana
roman.celin@imt.si

The connecting rod converts the piston's reciprocating motion into the rotary motion of the crankshaft. During service, connecting rods are subjected to a various loads. In the case of the connecting rod investigated here, the failure occurred after just 20,000 km on the car's odometer (approximately 2 years of service). The paper describes the results of an analysis of the fractured connecting rod's shank.

Keywords: connecting rod, nodular cast iron, failure, metallographic examination

Ojnica motorja z notranjim zgorevanjem pretvarja recipročno gibanje bata v krožno gibanje ročične gredi. Med obratovanjem so ojnice izpostavljena raznim obremenitvam. V primeru preiskovane ojnice se je prelom zgodil po le 20 000 prevoženih kilometrih (po približno dveh letih uporabe avtomobila). V članku so opisani razultati preiskave prelomljenega stebla ojnice.

Ključne besede: ojnica, nodularna litina, prelom, metalografska preiskava

1 INTRODUCTION

Connecting rods are generally manufactured using casting or forging, and in use support a variety of loads, such as [1]:

- compressive loading in the longitudinal direction, as a result of the gas pressure on the piston crown,
- alternate tensile and compressive loads, as a result of the changing piston velocity,
- bending loads in the connecting rod's shank, as a result of the oscillating motion about the gudgeon-pin axis,
- buckling stress, as a result of large compressive loads.

The frequency of alternating loading increases rapidly with an increase in the engine's rpm. In many cases a catastrophic engine failure is caused by a connecting-rod failure and sometimes the broken connecting rod's shank may even be pushed through the side of the crank-case, thereby rendering the engine irreparable. There are many reasons for such a failure, e.g., the overheating of the engine, cracking, deficiency of the bearing lubrication, poor maintenance, etc. A catastrophic failure occurred for one of the four connecting rods of a 1.8-litre 16-valve internal combustion car engine while travelling at 100 km/h on a motorway. The side of the crank-case was ruptured and the corresponding piston was very deformed. Both parts of the fractured connecting rod are shown in **Figure 1**.

2 EXAMINATION

The analysis of the fracture consisted of a visual examination, hardness measurements and a metallographic examination. The specimens for the metallographic and scanning electron microscope (SEM) examinations were cut from the connecting rod's shank

Figure 1: Connecting rod's fractured shank
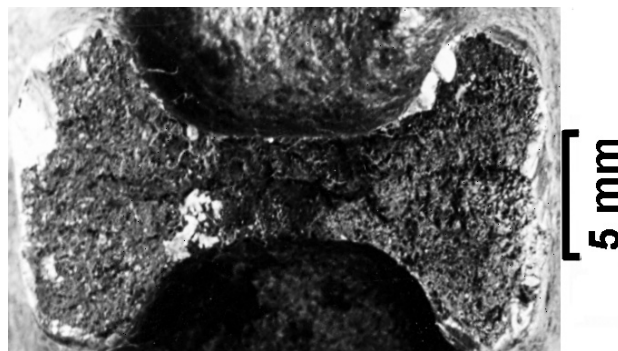**Slika 1:** Prelomljeno steblo ojnice

Figure 2: Fractured surface near the small end of the connecting rod's shank
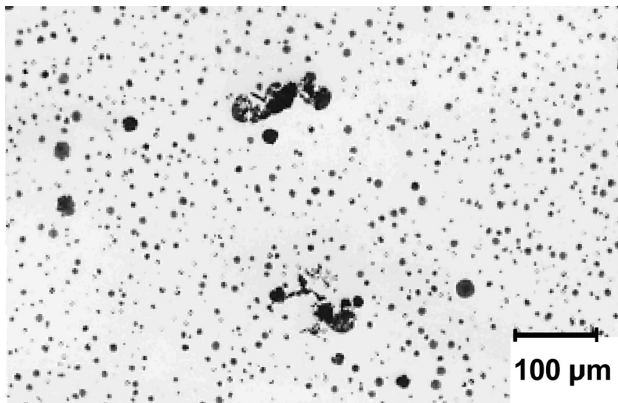**Slika 2:** Površina preloma na strani glave ojnice

Figure 3: Specimen's microstructure (unetched)
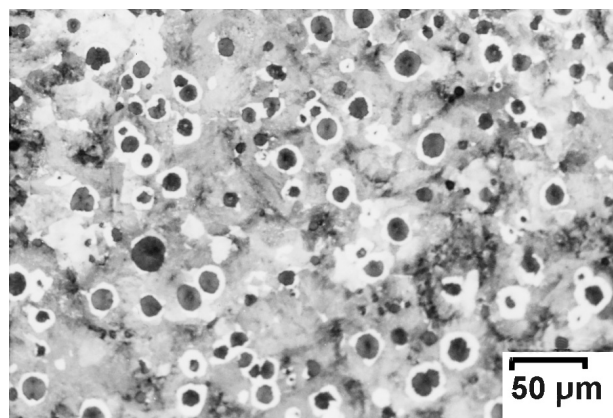**Slika 3:** Mikrostruktura vzorca ojnice (nejedkana)

Figure 4: Specimen's microstructure (nital etched)
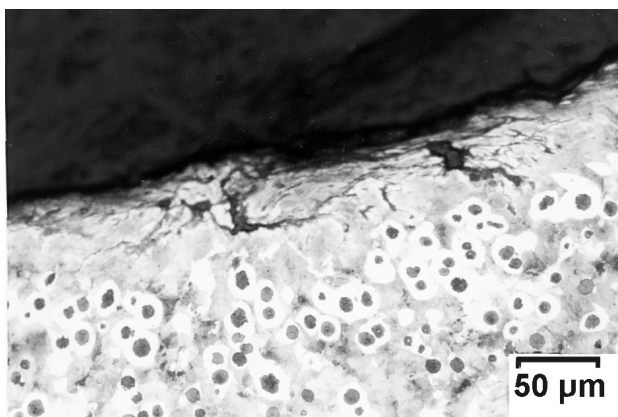**Slika 4:** Mikrostruktura jedkanega vzorca (nital)

Figure 5: Casting defect on the surface of the connecting rod
Slika 5: Livarska napaka na površini ojnice

near the fracture surface. The double-T cross-section of the shank's fractured surface is shown in **Figure 2**, and the rod's microstructure is shown in **Figure 3**.

The microstructure in **Figure 3** is typical for ductile iron (nodular graphite iron), with a fine lamellar pearlite matrix and small inserts of ferrite (approximately 5 %) around the graphite nodules (**Figure 4**).
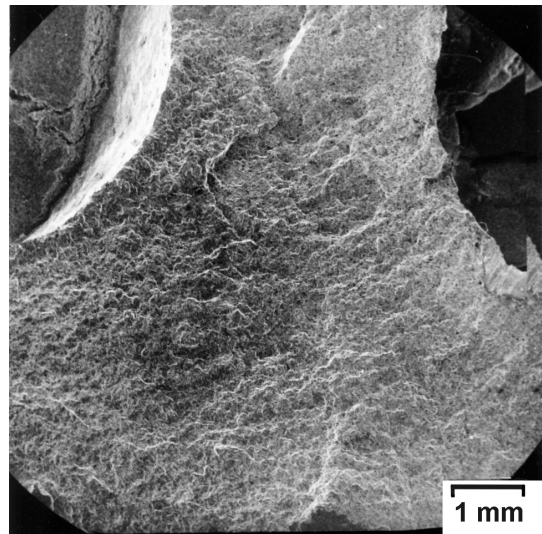

Figure 6: SEM image of the small-end fracture surface
Slika 6: SEM-posnetek preloma na strani glave ojnice

The whole surface of the connecting rod's two halves was examined carefully and numerous surface-casting defects were found. One of which is shown in **Figure 5**.

The fracture surface of the connecting rod was examined in the SEM, and the small-end fracture surface is shown in **Figure 6**.

3 RESULTS AND DISCUSSION

The connecting rod is made of pearlite ductile iron (nodular graphite cast iron), which is frequently used to substitute wrought or cast steel components. Examples of such a substitution include callipers and cylinders, turbochargers, connecting rods, etc. The benefits of using ductile iron in these applications are lower manufacturing costs [2].

According to the graphite classification, the microstructure in **Figure 3** corresponds to graphite form VI and graphite size 8 [3]. The graphite nodules are small
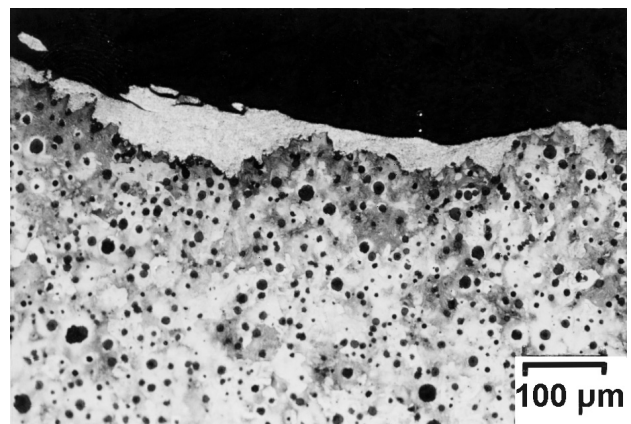

Figure 7: Residue of aluminium on the big-end fracture surface
Slika 7: Ostanki aluminija na površini preloma na strani noge ojnice
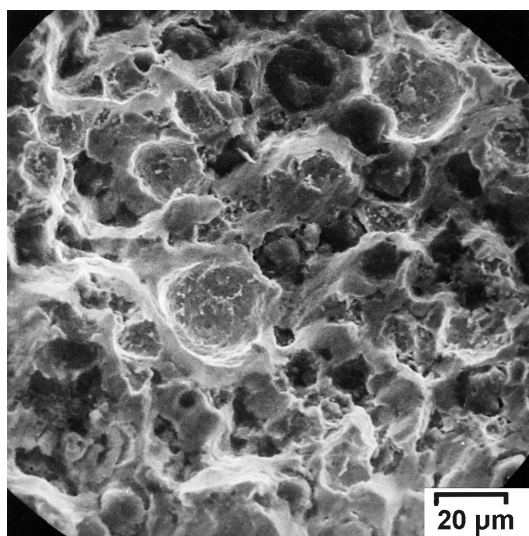
Figure 8: SEM image of small-end fracture surface
Slika 8: SEM-posnetek površine preloma pri glavi ojnice

(**Figure 3**), and this is evidence of an efficient process of nodulation with the probable addition of magnesium or cerium to the melt [4].

Figure 7 shows the microstructure of the big-end fracture surface. Residues of aluminium were found; a result of the connecting rod being pushed through the aluminium crank-case. The aluminium can be seen in **Figure 7** as structure on the edge of the fractured surface.

The surface of the connecting rod was sandblasted to increase the strength with strain hardening and to close the casting defects (**Figure 5**). The connecting rod supports a complex fatigue load, with repeated loading during every crankshaft revolution, and because of this loading, every casting defect has the potential to became the initial point for fatigue-crack initiation, where the local stress in the defect tip is increased because of the "notch effect". After an initial propagation, with each crack opening the crack advances by one striation, at a critical crack size the rupture occurs. On the investigated fracture surface the striations were not sufficiently clear to reliably determine the initiation point. The final fracture surface has marks of plastic straining and from their microscopic appearance it is concluded that the final fracture occurred with a very small plastic deformation preceding the opening of the crack. The final

rupture was, thus, very severe. At a low rate of separation the loose graphite nodules would be crushed and deposited on the fracture surface's dark-grey region [5]. Such regions were not detected on the examined sample.

The small end of the connecting rod's fracture surface was examined with the SEM. On the fracture surface there are numerous dimples with embedded graphite nodules or where the nodules had fallen out (**Figure 8**).

The HB hardness was measured on the connecting rod's shank. The measured value of 280 HB corresponds to pearlite ductile iron.

4 CONCLUSION

The fractured connecting rod had a microstructure of pearlite ferrite ductile iron with a normal size and shape of graphite nodules as well as a normal hardness of 280 HB. The share of ferrite is approximately of 5 %. The morphology of the fracture surface indicates that the fracture occurred instantaneously. Near the fracture surface several casting defects with a shape partially changed by sandblasting were found on the connecting rod's shank. It is concluded that one of these casting defects was probably the initiation point for the connecting-rod shank's fracture. Connecting rods made of ductile cast iron must have proper mechanical properties and microstructural characteristics, and should be without any manufacturing defects, because ductile iron is a notch-sensitive material. The rapid in-service failure of the examined connecting rod with surface defects is clear evidence that the foundry's and/or the engine manufacturer's quality control were in this case insufficient to detect the surface defects and prevent the use of the connecting rod in the car's engine.

5 REFERENCES

[1] Fisher R. et al. Modern Automotive Technology. Haan-Gruiten: Europa Lehrmittel; 2006
[2] ASM handbook, vol. 15, Casting. ASM International, Materials Park, OH 1998, p. 1454
[3] Designation of microstructure of cast irons ISO/DIS 945-1, 2006
[4] Brandes E. A., Brook G. B. Smithells, Metals Reference Book. Oxford: Butterworth Heinemann; 1999, 26–81
[5] Jen K., Scardina J. T., Smith D. G. Fractographic analysis of an ASTM as-cast pearlitic nodular iron. Metallography (**1986**) 3, 359–370